Structural and thermal properties of orientationally ordered dipolar fluids

B. Groh and S. Dietrich
Fachbereich Physik, Bergische Universität Wuppertal, D-42097 Wuppertal, Federal Republic of Germany
(Received 12 September 1995)

At high densities dipolar fluids with strong dipole moments exhibit an orientationally ordered phase. Using a density-functional theory for the corresponding Stockmayer model we study the properties of this ferromagnetic phase both in the absence of and as a function of an external field. In a needle-shaped volume the magnetization is homogeneous due to the lack of a demagnetization field. For other sample shapes in zero field inhomogeneous magnetization distributions are formed, leading to a shape-independent free energy that equals that of the needle-shaped volume. We discuss general properties of the resulting domain configurations and analyze some simple special cases in more detail. In an external field a phase transition occurs between homogeneously and inhomogeneously magnetized states, resulting in phase diagrams that depend on the shape of the sample.

PACS number(s): 64.70.−p, 75.50.Mm, 61.30.Gd, 75.60.−d

I. INTRODUCTION

Dipolar fluids consist of particles which carry a permanent dipole. They can be either molecules with an electric dipole moment or ferromagnetic colloidal particles suspended in a solvent forming a ferrofluid. Such fluids can exhibit long-ranged orientational order which is either due to spontaneous symmetry breaking or induced by the application of an external electric or magnetic field.

The first possibility was found first by Wei and Patey [1,2] in a Monte Carlo simulation of a dipolar soft sphere fluid. Meanwhile a ferroelectric phase has also been detected in dipolar hard spheres [3–5] and Stockmayer fluids [6]. In our previous work [7,8] we analyzed this phase in the framework of a density-functional theory which allowed us to calculate full phase diagrams that show interesting topological features. This analysis was restricted to a homogeneous spontaneous polarization which leads to a shape-dependent free energy. However, based on general arguments one expects that inhomogeneous polarization distributions lower the free energy, rendering it shape independent [9,10]. In the present paper we discuss this domain formation, which in fluids differs from the analogous problem in solids in that the anisotropy energy induced by the crystal structure vanishes, so that the domain wall thickness is expected to scale with the system size [11].

As far as the external field is concerned in the following we adopt the magnetic language, assuming that the particles carry *magnetic* dipole moments of magnitude m because the main application we have in mind is ferrofluids. In these systems it is much easier to observe appreciable field-dependent effects than in molecular dipolar fluids. For typical ferrofluids ($m \simeq 10^{-19}$ A m^2) the ratio of the field energy and the thermal energy, mH/k_BT, can be of order 1 for easily attainable field strengths ($\mu_0 H \simeq 0.042$ T) whereas for water with a dipole moment 1.82 D one would need an electrical field of 7×10^8 V/m to achieve the same effect. It should be pointed out that, in contrast to ferromagnetism induced by short-ranged forces, the effect of an external field on the continuous paramagnetic-ferromagnetic transition in dipolar systems is gentler, because due to the domain formation it shifts but does not destroy this transition [12,13].

In a needle-shaped sample the magnetization is homogeneous, whereas for other sample shapes the demagnetization field causes an inhomogeneous distribution of the magnetization. The first case without an external field has been thoroughly discussed in Ref. [8]. Here, in Sec. II, we study the influence of an external field on needle-shaped samples of dipolar fluids. In Sec. III we demonstrate the shape independence of the phase diagram in zero field for other sample shapes and characterize the class of possible domain configurations. By calculating the surface free energy we determine the most favorable configuration among those with sharp domain boundaries. Although in view of Ref. [11] configurations with sharp domain boundaries will certainly not correspond to the absolute minimum of the free energy, it is nonetheless very instructive to sort out which of those with this constraint is the most favorable one. Section IV deals with the influence of an external field for samples with finite aspect ratios. In Sec. V it is shown that the stripe and bubble domain structures, which usually occur in dipolar Ising systems [14], are unstable in dipolar fluids.

II. HOMOGENEOUS MAGNETIZATION IN AN EXTERNAL FIELD

In this section we extend the density-functional theory of Ref. [8] to the case of a homogeneously magnetized ellipsoid in an external field. First we give a brief outline of the density-functional theory for the liquid ferromagnetic phase developed in Ref. [8] in order to be able to discuss the field dependence. The dipolar fluid is described by the particle density $\hat{\rho}(\mathbf{r},\omega)$, which depends on the location $\mathbf{r}$ and the orientation ω of the particles. For fluid phases the number density $\rho = \int d\omega\, \hat{\rho}(\mathbf{r},\omega)$ is spatially

constant and $\alpha(\mathbf{r},\omega)=\hat{\rho}(\mathbf{r},\omega)/\rho$ is the orientational probability distribution at the point $\mathbf{r}$. Within the density-functional approach developed in Refs. [15,8] the grand canonical functional divided by the volume V of the sample is given by

$$\frac{1}{V}\Omega[\rho,\{\alpha(\mathbf{r},\omega)\},T,\mu]$$

$$=f_{\mathrm{HS}}(\rho)+\frac{\rho}{\beta}S+\frac{1}{V}\Omega_{\mathrm{int}}-\mu\rho+\frac{1}{V}\Omega_H\ , \quad (2.1)$$

where μ is the chemical potential, $\beta=1/(k_BT)$, and f_{HS} is the free energy density of an appropriate hard sphere reference system. The term

$$S=\frac{1}{V}\int d^3r\int d\omega\,\alpha(\mathbf{r},\omega)\ln[4\pi\alpha(\mathbf{r},\omega)] \quad (2.2)$$

takes into account the loss of entropy if the orientational distribution is not isotropic, i.e., equal to $1/(4\pi)$. The interaction contribution due to the long-range part of the pair potential between the spherical particles with embedded pointlike dipoles is

$$\Omega_{\mathrm{int}}=\frac{\rho^2}{2\beta}\int_V d^3r\int_V d^3r'\int d\omega\,d\omega'\alpha(\mathbf{r},\omega)\alpha(\mathbf{r}',\omega')\Theta(|\mathbf{r}-\mathbf{r}'|-\sigma)(1-e^{-\beta[w_{\mathrm{dip}}(\mathbf{r}-\mathbf{r}',\omega,\omega')+w_{\mathrm{LJ}}(|\mathbf{r}-\mathbf{r}'|)]}) \quad (2.3)$$

with the Lennard-Jones potential

$$w_{\mathrm{LJ}}(r)=4\epsilon\left[\left(\frac{\sigma}{r}\right)^{12}-\left(\frac{\sigma}{r}\right)^{6}\right] \quad (2.4)$$

and the dipolar potential

$$w_{\mathrm{dip}}(\mathbf{r}_{12},\omega,\omega')$$

$$=\frac{m^2}{r_{12}^3}\{\hat{\mathbf{m}}(\omega)\hat{\mathbf{m}}(\omega')-3[\hat{\mathbf{m}}(\omega)\hat{\mathbf{r}}_{12}][\hat{\mathbf{m}}(\omega')\hat{\mathbf{r}}_{12}]\}\ , \quad (2.5)$$

where m is the absolute value of the dipole moment $\mathbf{m}(\omega)$; $\hat{\mathbf{m}}(\omega)=\mathbf{m}(\omega)/m$, $\mathbf{r}_{12}=\mathbf{r}-\mathbf{r}'$, and $\hat{\mathbf{r}}_{12}=\mathbf{r}_{12}/r_{12}$. If the volume V has the shape of a rotational ellipsoid with aspect ratio k and if the magnetization is homogeneous, $\alpha(\mathbf{r},\omega)$ depends only on the angle θ relative to the long axis of the ellipsoid and thus can be expanded in Legendre polynomials:

$$2\pi\alpha(\omega)=\bar{\alpha}(\cos\theta)=\sum_{l=0}^{\infty}\alpha_lP_l(\cos\theta)\ ,$$
$$\alpha_l=\frac{2l+1}{2}\int_{-1}^{1}dx\,\bar{\alpha}(x)\ . \quad (2.6)$$

The magnetization is $M=\frac{2}{3}m\rho\alpha_1$. Using this expansion a careful analysis of the thermodynamic limit yields [8]

$$\frac{\Omega_{\mathrm{int}}}{V}=\rho^2\sum_{l=0}^{\infty}u_l\alpha_l^2\ , \quad (2.7)$$

where the explicit expressions for the coefficients u_l are given in Eqs. (3.23) and (3.24) in Ref. [8]. In particular one has [see Eqs. (3.26) and (4.10) in Ref. [8]]

$$u_1=\frac{8\pi}{9}[\tfrac{1}{3}-D(k)]m^2+O(m^6) \quad (2.8)$$

with the demagnetization factor

$$D(k)=-1/(k^2-1)+k/(k^2-1)^{3/2}\ln(k+\sqrt{k^2-1})$$

for $k>1$.

The additional energy in the presence of an external field H is

$$\Omega_H=-mH\int d^3r\,d\omega\,\hat{\rho}(\mathbf{r},\omega)\cos\theta\ , \quad (2.9)$$

where the angle θ is measured relative to the field direction. If this direction does not coincide with the direction of the *spontaneous* magnetization for $H=0$, i.e., the long axis of the ellipsoid, the field will tend to rotate the direction of the magnetization. We shall discuss an example thereof in Sec. IV. Here we restrain ourselves to the simpler case of an external field parallel to the homogeneous spontaneous magnetization which gives $\Omega_H/V=-\frac{2}{3}\rho mH\alpha_1$. The equilibrium configuration for given values of the temperature and chemical potential is determined by minimizing the density functional with respect to the density ρ and the orientational distribution $\bar{\alpha}(x)$ leading to the coupled equations

$$\frac{\partial f_{\mathrm{HS}}(\rho)}{\partial\rho}+\frac{1}{\beta}\int dx\,\bar{\alpha}(x)\ln[2\bar{\alpha}(x)]$$
$$+2\rho\sum_{l=0}^{\infty}u_l\alpha_l^2-\tfrac{2}{3}mH\alpha_1-\mu=0 \quad (2.10)$$

and

$$\bar{\alpha}(x)=\frac{\exp[-\beta\rho\sum_{l=1}^{\infty}(2l+1)u_l\alpha_lP_l(x)+\beta mHx]}{\int_{-1}^{1}dx\exp[-\beta\rho\sum_{l=1}^{\infty}(2l+1)u_l\alpha_lP_l(x)+\beta mHx]}\ , \quad (2.11)$$

which reduce to Eqs. (4.15) and (4.20) in [8] for $H=0$. According to Eq. (2.11) $\bar{\alpha}(x)$ is of the form

$$\bar{\alpha}(x)=C\exp[\gamma_1x+\gamma_2P_2(x)+\cdots]\ . \quad (2.12)$$

Equation (2.11) leads to the following system of equations for the parameters C and γ_l:

$$C^{-1}=\int_{-1}^{1}dx\exp\left[\sum_{i=1}^{\infty}\gamma_iP_i(x)\right]\ ,$$
$$\gamma_l=-\frac{(2l+1)^2}{2}\beta\rho u_lC\int_{-1}^{1}dx\,P_l(x)\exp\left[\sum_{i=1}^{\infty}\gamma_iP_i(x)\right]\ ,$$
$$l\geq 2\ , \quad (2.13)$$

and

$$\gamma_1 = -\tfrac{9}{2}\beta\rho u_1 C \int_{-1}^{1} dx\, x \exp\left[\sum_{i=1}^{\infty} \gamma_i P_i(x)\right] + \beta m H \ . \tag{2.14}$$

As in Ref. [8] only a finite number of terms appears in the summations if the coefficients u_l are expanded in powers of m^2 and then truncated at a sufficiently large order. Therefore the function $\bar{\alpha}(x)$ and the phase diagrams can be calculated following the same lines as in the zero field case.

In the following the variables will be given in reduced units:

$$T^* = k_B T/\epsilon, \quad \rho^* = \rho\sigma^3, \quad m^* = m/\sqrt{\sigma^3\epsilon}\ ,$$
$$H^* = H\sqrt{\sigma^3/\epsilon}, \quad M^* = M\sqrt{\sigma^3/\epsilon}\ . \tag{2.15}$$

The magnetization curves obtained from the numerical solution of Eqs. (2.13) and (2.14) for a needle-shaped sample, i.e., for aspect ratio $k = \infty$, where the demagnetization factor is zero, are displayed in Fig. 1 together with the result of the Langevin theory. The latter ignores the interactions between the particles and gives, with the Langevin function $L(x) = \coth x - 1/x$,

$$\alpha_1 = \tfrac{3}{2} L(\beta m H)\ , \tag{2.16}$$

which is independent of the density. The actual solution reduces to the Langevin theory in the limit $\rho \to 0$. However, at higher densities the particle interactions lead to an increase of the magnetization and the zero field susceptibility. Finally, at densities above the ferromagnetic critical point $\rho_{fc}(T)$ [see Eq. (7.10) in Ref. [8]] the fluid exhibits a spontaneous magnetization. The phase diagrams in the density-temperature plane are presented in Fig. 2 for various fixed values of the magnetic field and for the reduced dipole moment $m^* = 1.5$. As the field increases the critical point of the liquid-gas transition is shifted to higher densities and higher temperatures because the nonzero orientational order of the particles induced by the field even at high temperatures and low densities leads to a stronger effective interaction. Since for $k = \infty$ there is only a single domain the second order phase transition between the ferromagnetic and the isotropic liquid phase at $H = 0$ is smeared out by the external field, but it leaves fingerprints at nonzero field, e.g., for weak fields the susceptibility exhibits a pronounced maximum near the loci of the second order transitions at $H = 0$ (see Fig. 3). The tricritical point turns into a critical point whose corresponding critical density decreases with increasing strength of the field. As function of H its corresponding critical temperature first decreases and then increases again (see Fig. 4). For strong fields the critical points of the liquid-gas transition and of the isotropic-ferromagnetic transition merge so that only a single critical point is left. A similar series of phase diagrams was found by Zhang and Widom [10] based on a phenomenological model, whereas our results follow from a microscopic approach. Figure 5 represents the field dependence of the critical temperature and density corresponding to the liquid-gas transition. In accordance with Ref. [16] we find that the critical quantities increase

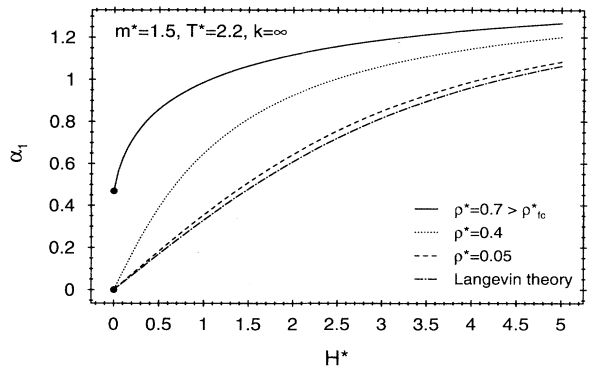

FIG. 1. Typical magnetization curves ($M = \frac{2}{3}\rho m \alpha_1$) in a needle-shaped sample ($k = \infty$) for different values of the reduced density ρ^*. The Langevin theory [see Eq. (2.16)], which ignores the particle interactions, is a good approximation only at low densities. For $\rho > \rho_{fc}(T)$ $M(H \to 0)$ is nonzero which corresponds to a spontaneous magnetization. For $\rho < \rho_{fc}(T)$ one has $M(H \to 0) = 0$ and there is no spontaneous magnetization.

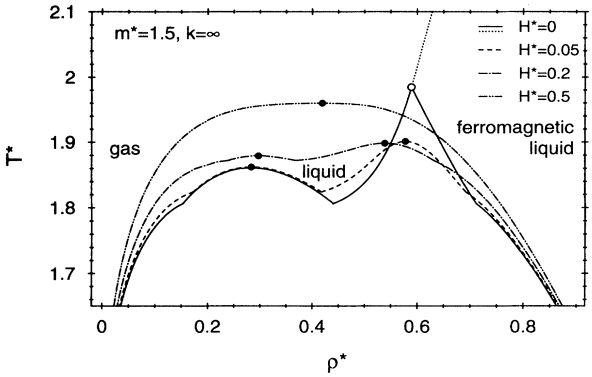

FIG. 2. Evolution of the phase diagram with the external field for a dipolar fluid in a needle-shaped container for $m^* = 1.5$. At low temperatures there is a first order transition between a gas and a ferromagnetic liquid. For small H there is a triple temperature above which one has a first order transition between a gas and a liquid as well as a first order transition between a liquid and a ferromagnetic liquid, which both end in a critical point denoted by the full dots. For $H = 0$ the latter transition ends in a tricritical point (open circle) above which this transition persists as a continuous transition along a line of critical points (dotted line) which is eliminated for $H \neq 0$. The tricritical point turns into a critical point for $H \neq 0$. For strong fields the critical points merge and one has only one first order transition between an isotropic gas and a ferromagnetic liquid with a single critical point. The liquid phase and the ferromagnetic liquid phase differ in that for $H = 0$ the former phase is isotropic whereas the latter phase is ferromagnetically ordered. For $H \neq 0$ all phases exhibit a nonzero magnetization.

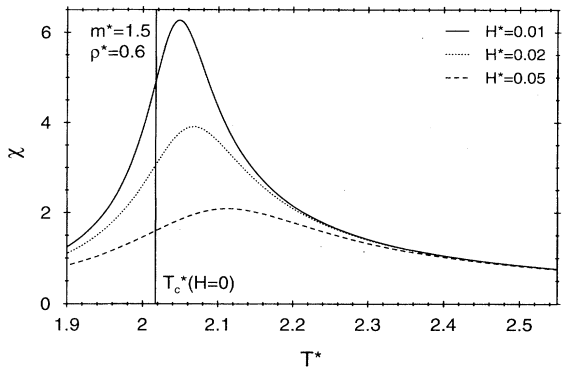

FIG. 3. The susceptibility $\chi=\partial M/\partial H$ as a function of the temperature for a needle-shaped sample in finite fields. The pronounced maxima for small fields near the critical temperature $T_c^*(\rho^*=0.6, H=0)=2.017$ are fingerprints of the divergence of the susceptibility at the transition point in zero field. For temperatures $T^* \gg 2.5$ all curves approach the susceptibility $\chi=\frac{1}{3}\beta\rho m^2+O(H^2)$ that can be derived from the Langevin theory [see Eq. (2.16)].

quadratically with H at low fields. The corresponding amplitude increases strongly with the dipole moment due to the influence of the second critical point stemming from the isotropic-ferromagnetic transition. Boda, Szalai, and Liszi [16] do not find the ferromagnetic phase or the second critical point but the flattening of the coexistence curve at high densities which they observe may be caused by the influence of that phase. Insofar as they do not specify the shape of the sample their theory seems to be incomplete.

In the following we present a detailed comparison with

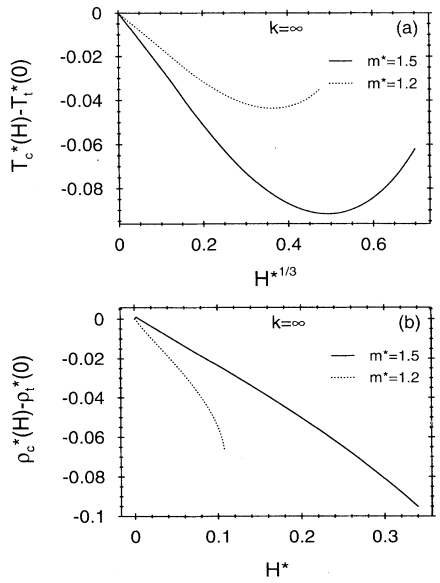

FIG. 4. Shift of the temperature and density of the liquid–ferromagnetic-liquid critical point as a function of the applied field. For small fields we find that the shift of the temperature is proportional to $H^{1/3}$ and the shift of the density is linear in H.

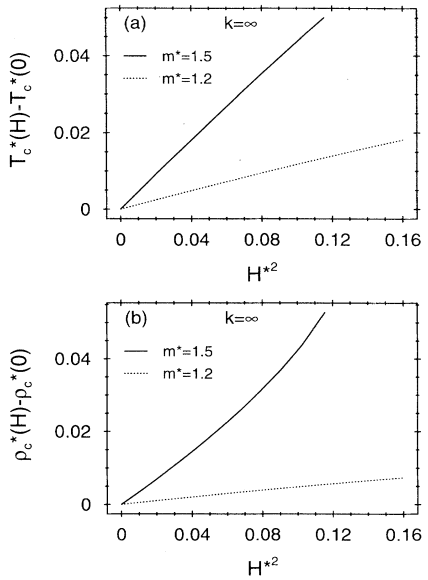

FIG. 5. Shift of the critical temperature and of the critical density of the liquid-gas critical point as a function of the applied field for two different values of the dipole moment. For small H both shifts increase quadratically as a function of H.

the results of the Monte Carlo simulations of Stockmayer fluids in external fields by Stevens and Grest [6]. Note that the infinitely permeable surrounding they used completely suppresses the demagnetization field and thus is equivalent to the limit of a needle-shaped sample (see Sec. III in Ref. [8]). The main difference from our results is that in the simulations the transition to the ferromagnetic phase is found only at very high densities and dipole moments, e.g., for $m^*=2.5$ and $T^*=1.5$ they estimate $\rho_{fc}^*=0.9$. (They are not able to determine the order of the phase transition.) If this can be corroborated it indicates that for large dipole moments our approach overestimates the stability of the orientationally ordered phase. On the other hand, in contrast to the simulations, which allow one to explore only a small portion of the parameter space, we are able to determine full phase diagrams, which exhibit interesting topological features. Stevens and Grest observe that their data for the relative increase of the critical temperature $T_c(H)/T_c(0)$ plotted as function of the quantity $m^*H^*/[T_c(H)/T_c(0)]$ approximately lie on a straight line which is independent of m^*. Figure 6 shows that our data rather lie on an S-shaped curve, which seems to be also consistent with the simulation data, and that the results for different m^* do not scale. As a consequence of the overestimation of the stability of the ferromagnetic phase for dipole moments as high as $m^*=2.5$ we do not find a critical point in zero field for this value of m^* [see Fig. 15(a) in Ref. [8]]. The critical point at $H\neq 0$ which evolves from the tricritical point does not have much in common with the liquid-gas-like critical point found in the simulations, e.g., at $H^*=0.5$ we find $\rho_c^*=0.5012$ and $T_c^*=4.562$ while from Ref. [6] $\rho_c^*=0.285$ and $T_c^*=2.71$. Therefore in Figs. 6 and 7 we refrain from a comparison of the results for

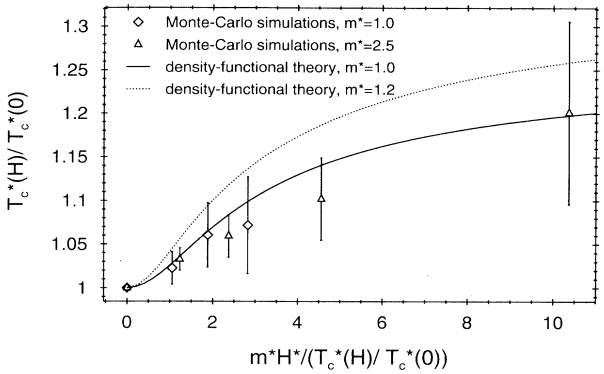

FIG. 6. The critical temperature of the liquid-gas critical point as a function of the external field using the scaled variables introduced by Stevens and Grest [6]. The symbols are the results of their Monte Carlo simulation whereas the lines are obtained from the present theory. While Stevens and Grest infer from their data a linear relationship, we find a quadratic behavior at low fields (see Fig. 5) and a saturation at high fields. Furthermore, we do not observe scaling. Within the framework of the present density-functional theory for $m^*=2.5$ the influence of the ferromagnetic phase on the phase diagram is already so strong that it wipes out the liquid-gas critical point so that there is no $T_c(0)$ anymore.

$m^*=2.5$. The phase diagrams for small dipole moments compare favorably with those obtained by the simulations; the overestimation of the liquid densities at low temperatures can be traced back to the low-density approximation of the correlation function used in our approach [15]. Compared with the simulation data the density-functional theory provides better access to the critical points albeit in terms of classical critical exponents. However, at least at present the expected nonclassical behavior of these systems seems to be out of reach for the simulations. In Fig. 7 we compare the results for the reduced magnetization $M/(\rho m)=\frac{2}{3}\alpha_1$ at the critical point as a function of the external field. For $m^*=1.0$ the agreement is quite satisfactory, whereas, as noted above, a comparison at $m^*=2.5$ does not make sense.

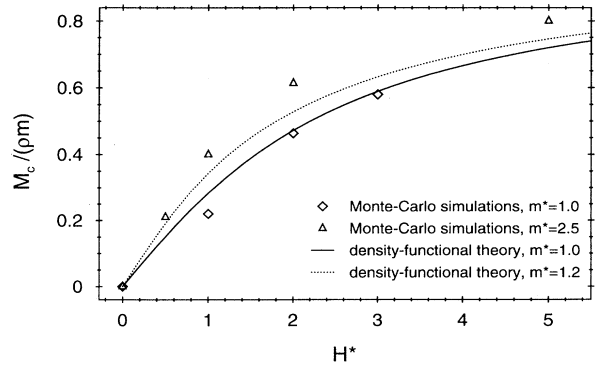

FIG. 7. Reduced magnetization $M/(\rho m)=\frac{2}{3}\alpha_1$ at the liquid-gas critical point versus the external field, as obtained by Monte Carlo simulations [6] (symbols) compared with the results of the present density-functional theory (lines).

III. DOMAIN STRUCTURE IN ZERO FIELD

A. General aspects

As already pointed out in Ref. [8] for finite aspect ratios of the sample the formation of domains lowers its free energy as compared to the homogeneously magnetized state. For dipoles on a lattice Griffiths [9] has proven that this leads to a *shape-independent* free energy in the thermodynamic limit as long as no external field is applied. We want to show that, in the framework of our approach, this statement can be extended to dipolar fluids. To this end we identity the class of domain configurations which minimize the bulk contribution to the grand canonical functional and show that they have the same free energy as the homogeneously magnetized long needle ($k\rightarrow\infty$). Consequently the phase diagrams obtained for this case (see Fig. 15 in Ref. [8]), for which the homogeneous state *is* the one with the lowest free energy, are valid for any sample shape.

The actual orientational distribution can be expanded in a reference frame fixed in space:

$$\alpha(\mathbf{r},\omega)=\sum_{l=0}^{\infty}\sum_{m=-l}^{l}\mu_{lm}(\mathbf{r})Y_{lm}(\omega)\ , \tag{3.1}$$

where $\mu_{00}=1/\sqrt{4\pi}$ due to the normalization $\int d\omega\,\alpha(\mathbf{r},\omega)=1$ and $\mu_{lm}^*=(-1)^m\mu_{l\overline{m}}$ since α is real. (Here and in the following $\overline{m}=-m$.) In order to study the domain formation, here we consider only such configurations which scale with the system size. This means that for large system sizes L the coefficients μ_{lm} depend on the three lengths $\mathbf{r}$, σ, and L only via $\mathbf{r}/L$:

$$\mu_{lm}(\mathbf{r},\sigma,L)=\mu_{lm}^{(0)}(\mathbf{r}/L),\quad L/\sigma\rightarrow\infty\ . \tag{3.2}$$

This scaling certainly does not hold near the surface of the sample, but these deviations are expected to occur only in a surface layer whose thickness is not proportional to L so that they can be neglected for the bulk contribution to Ω.

In the following we derive a simple expression for the interaction contribution $\Omega_{\rm int}$ [Eq. (2.3)] for configurations satisfying Eq. (3.2). Using Eq. (3.1) and the expansion of the Mayer function in terms of rotational invariants,

$$\Phi_{l_1l_2l}(\omega,\omega',\omega_{12})=\sum_{m_1,m_2,m}C(l_1l_2l,m_1m_2m)Y_{l_1m_1}(\omega)\times Y_{l_2m_2}(\omega')Y_{lm}^*(\omega_{12})\ , \tag{3.3}$$

with the Clebsch-Gordan coefficients $C(l_1l_2l,m_1m_2m)$ in the notation of Rose [17] and Gray and Gubbins [18] (see Ref. [8]),

$$\Theta(r_{12}-\sigma)(e^{-\beta[w_{\rm dip}(\mathbf{r}_{12},\omega,\omega')+w_{\rm LJ}(r_{12})]}-1)=\sum_{l_1,l_2,l}\hat{f}_{l_1l_2l}(r_{12})\Phi_{l_1l_2l}(\omega,\omega',\omega_{12})\ , \tag{3.4}$$

[note that for $\hat{f}_{l_1l_2l}$ to be nonzero both l_1+l_2 and l must be even (see Appendix B in Ref. [15])] Eq. (2.3) can be written as

$$\Omega_{\rm int}=-\frac{\rho^2}{2\beta}\sum_{l_1,l_2,l}\sum_{m_1,m_2,m}C(l_1l_2l,m_1m_2m)\int_V d^3r\int_V d^3r'\mu_{l_1m_1}(\mathbf{r})\mu_{l_2m_2}(\mathbf{r}')\hat{f}_{l_1l_2l}(r_{12})Y_{lm}(\omega_{12})$$

$$=-\frac{\rho^2}{2\beta}\sum_{l_1,l_2,l}\sum_{m_1,m_2,m}C(l_1l_2l,m_1m_2m)\int_V d^3r\,\mu_{l_1m_1}(\mathbf{r})\int_{V_s(\mathbf{r})}d^3r_{12}\mu_{l_2m_2}(\mathbf{r}-\mathbf{r}_{12})\hat{f}_{l_1l_2l}(r_{12})Y_{lm}(\omega_{12}) \tag{3.5}$$

with the shifted volume

$$V_s(\mathbf{r})=\{\mathbf{x}\in\mathbb{R}^3|\mathbf{x}=\mathbf{r}-\mathbf{y},\mathbf{y}\in V\}\ .$$

Here and in the following the summations over l_1, l_2, l, m_1, m_2, and m are to be taken as [8]

$$\sum_{l_1,l_2,l}\sum_{m_1,m_2,m}\cdots=\sum_{l_1=0}^{\infty}\sum_{l_2=0}^{\infty}\sum_{l=0}^{\infty}\sum_{m_1=-l_1}^{l_1}\sum_{m_2=-l_2}^{l_2}\sum_{m=-l}^{l}\cdots\ . \tag{3.6}$$

First we consider all "short-ranged" (SR) contributions to the coefficients $\hat{f}_{l_1l_2l}(r_{12})$ that vanish $\sim r_{12}^{-6}$ or faster for large distances r_{12}. We introduce the scaled variables $\mathbf{x}=\mathbf{r}/L$ and $\mathbf{x}_{12}=\mathbf{r}_{12}/L$ and use the expansion $\hat{f}^{(\rm SR)}_{l_1l_2l}(r)=\sum_{n=6}^{\infty}c_n^{(l_1l_2l)}r^{-n}$, which yields

$$\Omega^{(\rm SR)}_{\rm int}=-\frac{\rho^2}{2\beta}\sum_{l_1,l_2,l}\sum_{m_1,m_2,m}C(l_1l_2l,m_1m_2m)\sum_{n=6}^{\infty}L^{6-n}c_n^{(l_1l_2l)}\int_{\tilde{V}}d^3x\,\mu^{(0)}_{l_1m_1}(\mathbf{x})$$

$$\times\int d\omega_{12}Y_{lm}(\omega_{12})\int_{\sigma/L}^{g(\omega_{12})}dx_{12}x_{12}^{2-n}\mu^{(0)}_{l_2m_2}(\mathbf{x}-\mathbf{x}_{12})\ . \tag{3.7}$$

Here $\tilde{V}=L^{-3}V$ is the scaled volume and the function $g(\omega_{12})$ defines the surface of the scaled region of integration $L^{-3}V_s$. When the expansion

$$\mu^{(0)}_{l_2m_2}(\mathbf{x}-\mathbf{x}_{12})=\mu^{(0)}_{l_2m_2}(\mathbf{x})-\mathbf{x}_{12}\cdot\nabla\mu^{(0)}_{l_2m_2}(\mathbf{x})+\cdots \tag{3.8}$$

is introduced the evaluation of the radial integration shows that the gradient and higher-order terms do not contribute to the bulk term so that $\mu^{(0)}_{l_2m_2}(\mathbf{x}-\mathbf{x}_{12})$ can be replaced by $\mu^{(0)}_{l_2m_2}(\mathbf{x})$. Then the angular integration over ω_{12} yields $l=0$, $m=0$, and therefore $l_1=l_2$, $m_1=-m_2$ so that the bulk term is given by

$$\lim_{L\to\infty}\frac{\Omega^{(\rm SR)}_{\rm int}}{L^3}=-\frac{\rho^2}{2\beta}\sum_{lm}C(ll0,m\bar{m}0)\sum_{n=6}^{\infty}c_n^{(ll0)}(-\sigma^{-3-n})$$

$$\times\int_{\tilde{V}}d^3x\,\mu^{(0)}_{lm}(\mathbf{x})\mu^{(0)}_{l\bar{m}}(\mathbf{x})\ . \tag{3.9}$$

By using

$$C(ll0,m\bar{m}0)=(-1)^{l+m}/\sqrt{2l+1}$$

in the thermodynamic limit the short-range contributions sum up to

$$\Omega^{(\rm SR)}_{\rm int}=\pi\rho^2\sum_{l=0}^{\infty}(2l+1)\hat{u}_l\sum_m\int_V d^3r|\mu_{lm}(\mathbf{r})|^2 \tag{3.10}$$

with the coefficients $\hat{u}_l$ given by

$$\hat{u}_l=-\frac{1}{\beta}\frac{(-1)^l}{\sqrt{\pi}(2l+1)^{3/2}}\int_\sigma^\infty dr\,r^2\hat{f}_{ll0}(r)\ . \tag{3.11}$$

One should note that $\hat{u}_l=u_l$ for $l\neq1$ [see Eq. (2.7)] and $\hat{u}_1=u_1+(8\pi/9)[\frac{1}{3}-D(k)]m^2$ [see Eq. (3.24) in Ref. [8]].

The only "long-ranged" (LR) contribution, stemming from the dipolar potential and decaying only $\sim r_{12}^{-3}$, appears in $\hat{f}_{112}$:

$$\hat{f}^{(\rm LR)}_{112}(r)=(4\pi)^{3/2}\sqrt{\tfrac{2}{15}}\frac{\beta m^2}{r^3}\ . \tag{3.12}$$

[The next-to-leading-order terms in $\hat{f}_{112}(r\to\infty)$ decay $\sim r^{-9}$ and thus can be treated as the other short-ranged terms. However, since for them $l\neq0$ they do not contribute to Eq. (3.10).] The corresponding contribution to $\Omega_{\rm int}$,

$$\Omega^{(\rm LR)}_{\rm int}=-\tfrac{1}{2}\rho^2m^2(4\pi)^{3/2}\sqrt{\tfrac{2}{15}}\sum_{m_1,m_2,m}C(112,m_1m_2m)$$

$$\times\int_V d^3r\int_V d^3r'\mu_{1m_1}(\mathbf{r})\mu_{1m_2}(\mathbf{r}')$$

$$\times r_{12}^{-3}Y_{2m}(\omega_{12})\ , \tag{3.13}$$

must be treated differently. By inserting the spherical harmonics and carrying out the summation it can be shown that $\Omega^{(\rm LR)}_{\rm int}$ can be cast into the form

$$\Omega^{(\rm LR)}_{\rm int}=\tfrac{1}{2}\sum_{ij}\int_V d^3r\int_V d^3r'M_i(\mathbf{r})T_{ij}(\mathbf{r}_{12})M_j(\mathbf{r}') \tag{3.14}$$

with the local magnetization

$$\mathbf{M}(\mathbf{r})=\left[\frac{4\pi}{3}\right]^{1/2}\rho m\begin{bmatrix}-\sqrt{2}\ \mathrm{Re}\mu_{11}(\mathbf{r})\\ \sqrt{2}\ \mathrm{Im}\mu_{11}(\mathbf{r})\\ \mu_{10}(\mathbf{r})\end{bmatrix} \tag{3.15}$$

and the dipole tensor

$$T_{ij}(\mathbf{r})=\Theta(r-\sigma)\left[\delta_{ij}-3\frac{r_i r_j}{r^2}\right]r^{-3}=\Theta(r-\sigma)\partial_j\frac{r_i}{r^3}\ . \tag{3.16}$$

Equation (3.14) can be rewritten as

$$\Omega_{\rm int}^{\rm (LR)}=-\tfrac{1}{2}\int_V d^3r\,\mathbf{M}(\mathbf{r})\cdot\mathbf{h}(\mathbf{r}) \tag{3.17}$$

with

$$h_j(\mathbf{r})=-\int_V d^3r'\Theta(r_{12}-\sigma)\mathbf{M}(\mathbf{r}')\cdot\nabla_{12}\left[\frac{(r_{12})_j}{r_{12}^3}\right]\ . \tag{3.18}$$

In the next step we establish the connection between this mean field, describing the influence of the magnetized fluid on a particle at point $\mathbf{r}$, and the demagnetization field $\mathbf{H}_d$ which is used in macroscopic and mesoscopic treatments of ferromagnetic materials and is defined by

$$\nabla\cdot\mathbf{H}_d=-4\pi\nabla\cdot\mathbf{M},\quad \nabla\times\mathbf{H}_d=\mathbf{0}\ . \tag{3.19}$$

From these equations one infers that $\mathbf{H}_d$ is the gradient of a scalar potential satisfying Poisson's equation so that standard reasoning shows that ($\mathbf{r}_{12}=\mathbf{r}-\mathbf{r}'$)

$$\begin{aligned}[H_d(\mathbf{r})]_j&=-\int_V d^3r'[\nabla'\cdot\mathbf{M}(\mathbf{r}')]\frac{(r_{12})_j}{r_{12}^3}+\oint_{\partial V}d^2\mathbf{n}'\cdot\mathbf{M}(\mathbf{r}')\frac{(r_{12})_j}{r_{12}^3}\\&=-\int_{V\setminus S_\sigma(\mathbf{r})}d^3r'[\nabla'\cdot\mathbf{M}(\mathbf{r}')]\frac{(r_{12})_j}{r_{12}^3}-\int_{S_\sigma(\mathbf{r})}d^3r'[\nabla'\cdot\mathbf{M}(\mathbf{r}')]\frac{(r_{12})_j}{r_{12}^3}\\&\quad+\int_{V\setminus S_\sigma(\mathbf{r})}d^3r'\nabla'\cdot\left[\mathbf{M}(\mathbf{r}')\frac{(r_{12})_j}{r_{12}^3}\right]+\oint_{\partial S_\sigma(\mathbf{r})}d^2\mathbf{n}'\cdot\mathbf{M}(\mathbf{r}')\frac{(r_{12})_j}{r_{12}^3}\ .\end{aligned} \tag{3.20}$$

In the last step Gauss's law has been applied for the volume $V\setminus S_\sigma(\mathbf{r})$ in which the integrand is regular. $\mathbf{n}'$ is the normal vector on the surface of V, i.e., ∂V, or of $S_\sigma(\mathbf{r})=\{\mathbf{x}\in\mathbb{R}^3\,|\,|\mathbf{x}-\mathbf{r}|\le\sigma\}$, i.e., $\partial S_\sigma(\mathbf{r})$, pointing outwards. The contributions from points $\mathbf{r}$ in a surface layer of thickness σ for which the above separation of V into $V\setminus S_\sigma(\mathbf{r})$ and $S_\sigma(\mathbf{r})$ is not possible can be neglected in the thermodynamic limit. Using the product rule we find that the first and third terms together just give $h_j(\mathbf{r})$. For the other two terms we again use the expansion [see Eqs. (3.2) and (3.8)]

$$\begin{aligned}M_j(\mathbf{r}')&=M_j(\mathbf{r}-\mathbf{r}_{12})\\&=M_j^{(0)}(\mathbf{r}/L)-\frac{\mathbf{r}_{12}}{L}\cdot\nabla M_j^{(0)}(\mathbf{r}/L)+\cdots\end{aligned} \tag{3.21}$$

and find that the second term in Eq. (3.20) is of order σ/L while the last term gives

$$-\mathbf{M}(\mathbf{r})\cdot\oint_{\partial S_\sigma(0)}d^2\mathbf{n}_{12}\frac{(r_{12})_j}{r_{12}^3}=-\frac{4\pi}{3}M_j(\mathbf{r})\ . \tag{3.22}$$

Thus we have shown that the demagnetization field and the mean field just differ by the field produced inside a homogeneously magnetized sphere (of radius σ) with magnetization $\mathbf{M}(\mathbf{r})$:

$$\mathbf{H}_d(\mathbf{r})=\mathbf{h}(\mathbf{r})-\frac{4\pi}{3}\mathbf{M}(\mathbf{r})\ . \tag{3.23}$$

From Eq. (3.17) one obtains

$$\Omega_{\rm int}^{\rm (LR)}=-\frac{1}{2}\int_V d^3r\,\mathbf{M}(\mathbf{r})\cdot\mathbf{H}_d(\mathbf{r})-\frac{2\pi}{3}\int_V d^3r\,\mathbf{M}^2(\mathbf{r})\ , \tag{3.24}$$

which can be rewritten as

$$\Omega_{\rm int}^{\rm (LR)}=\frac{1}{8\pi}\int_{\mathbb{R}^3}d^3r\,\mathbf{H}_d^2(\mathbf{r})-\frac{2\pi}{3}\int_V d^3r\,\mathbf{M}^2(\mathbf{r})\ . \tag{3.25}$$

[Equation (3.19) implies $\mathbf{M}=-1/(4\pi)\mathbf{H}_d+\nabla\times\mathbf{A}$ with $\nabla\times\nabla\times\mathbf{A}=\nabla\times\mathbf{M}$; $\nabla\cdot(\mathbf{H}_d\times\mathbf{A})=-\mathbf{H}_d\cdot(\nabla\times\mathbf{A})$ and Gauss's law lead to Eq. (3.25), because $\mathbf{H}_d$ decays as r^{-3} for $r\to\infty$.] We remark that if the magnetization is homogeneous throughout the sample one has [19]

$$\frac{1}{8\pi}\int_{\mathbb{R}^3}d^3r\,\mathbf{H}_d^2(\mathbf{r})=2\pi V\sum_{i,j}D_{ij}M_iM_j \tag{3.26}$$

with the generalized demagnetization factors D_{ij}. If the magnetization points along the z direction, the long-ranged interaction contribution is $\Omega_{\rm int}^{\rm (LR)}/V=2\pi(D_{33}-\frac{1}{3})M^2$. This is in accordance with our previous result in Ref. [8], because here $M=\frac{2}{3}\rho m\alpha_1$ and $D_{33}=D(k)$.

In summary we have found that for $H=0$ the bulk part of the grand canonical functional can be written as

$$\Omega^{(b)}=\int_V d^3r\,f(\mathbf{r})+\frac{1}{8\pi}\int_V d^3r\,\mathbf{H}_d^2(\mathbf{r})-\mu\rho V \tag{3.27}$$

with the free energy density

$$\begin{aligned}f(\mathbf{r})&=f_{\rm HS}(\rho)+\frac{\rho}{\beta}\int d\omega\,\alpha(\mathbf{r},\omega)\ln[4\pi\alpha(\mathbf{r},\omega)]\\&\quad+\pi\rho^2\sum_{l,m}(2l+1)\hat{u}_l|\mu_{lm}(\mathbf{r})|^2-\frac{2\pi}{3}\mathbf{M}^2(\mathbf{r})\ .\end{aligned} \tag{3.28}$$

Note that $f(\mathbf{r})$ is invariant under local rotations of the orientational distribution $\alpha(\mathbf{r},\omega)$ because under such transformations the coefficients μ_{lm} transform according to

$$\mu'_{lm}(\mathbf{r})=\sum_n D^l_{mn}[\Omega(\mathbf{r})]\mu_{ln}(\mathbf{r}) \tag{3.29}$$

where $D^l_{mn}[\Omega(\mathbf{r})]$ is a rotation matrix (see Sec. VI in Ref. [8]) and $\sum_m|\mu'_{lm}(\mathbf{r})|^2=\sum_m|\mu_{lm}(\mathbf{r})|^2$ is invariant. For $l=1$ this means that the absolute value of the local magnetization, $|\mathbf{M}(\mathbf{r})|$, does not change [see Eq. (3.15)]. The first term in Eq. (3.27) leads to the same minimum condition for the coefficients $\mu_{lm}(\mathbf{r})$ at each point $\mathbf{r}$. Since for $H=0$ locally there is no preferred direction the equilibrium configuration is axially symmetric, i.e., in a suitably chosen reference frame

$$\alpha(\mathbf{r},\omega)=\bar{\alpha}(\cos\theta)=\frac{1}{2\pi}\sum_{l=0}^{\infty}\alpha_l P_l(\cos\theta)\ . \tag{3.30}$$

When this ansatz is inserted into Eq. (3.28) one ends up with exactly the same minimization problem as for the needle-shaped sample for which

$$f(\mathbf{r})=f_{\mathrm{HS}}(\rho)+\frac{\rho}{\beta}\int_{-1}^{1}\bar{\alpha}(x)\ln[2\bar{\alpha}(x)] +\rho^2\sum_l\hat{u}_l\alpha_l^2-\frac{8\pi}{27}\rho^2m^2\alpha_1^2\ . \tag{3.31}$$

The preferential direction with respect to which the angle θ is measured may vary spatially in an arbitrary way. Obviously the second term in Eq. (3.27) takes on its minimum value zero for all configurations with vanishing demagnetization field. According to Eq. (3.20) this is the case if $\nabla\cdot\mathbf{M}=0$ everywhere in the sample and $\mathbf{n}\cdot\mathbf{M}=0$ on the surface. Thus we can conclude that the minimum of the total grand canonical functional is attained by those configurations that minimize both terms simultaneously, i.e., for those that are generated from the homogeneous configuration in a needle-shaped sample at the same values of the parameters ρ and T by spatially varying rotations in such a way that the conditions $\nabla\cdot\mathbf{M}=0$ and $\mathbf{n}\cdot\mathbf{M}=0$ at the surface are fulfilled. All these configurations have the same bulk contribution to the density functional, namely, that of the homogeneously magnetized long needle. This corroborates the validity of Griffiths's theorem within our approach also for dipolar fluids.

For such configurations $\nabla\times\mathbf{M}\neq\mathbf{0}$, i.e., there are closed magnetization lines; otherwise $\mathbf{M}$ would be the gradient of a potential Φ that satisfies Laplace's equation inside V with Neumann boundary conditions $\partial_n\Phi=0$ on the surface. But this problem has only the trivial solution $\mathbf{M}=\mathbf{0}$. A further corollary is that the average magnetization $\langle\mathbf{M}\rangle=V^{-1}\int d^3r\,\mathbf{M}(\mathbf{r})$ vanishes because one has

$$\int d^3r\,\mathbf{M}(\mathbf{r})\cdot\hat{\mathbf{e}}_i=\int d^3r\,\mathbf{M}(\mathbf{r})\cdot\nabla r_i =\int d^3r\,\nabla\cdot[r_i\mathbf{M}(\mathbf{r})]=\oint d^2\mathbf{n}\cdot\mathbf{M}(\mathbf{r})r_i=0\ . \tag{3.32}$$

B. Hexagonal, triangular, and trapezoidal domains in a cube

The most stable configurations within the above class can only be determined by comparing the corresponding surface contributions to the grand canonical potential. This is a very demanding task which, however, simplifies considerably if sharp domain boundaries are assumed with the magnetization being constant within each domain. In order to avoid sources of the demagnetization field, which according to Eq. (3.25) would increase the energy, the normal component of $\mathbf{M}$ has to be continuous at each domain boundary. As an example for a configuration which fulfills all the above conditions inside a cubic sample we examine the layered structure that is depicted in Fig. 8 and which is translationally invariant in the z direction. The small triangular domains prevent the existence of a magnetic surface charge density $\mathbf{M}\cdot\mathbf{n}\neq0$ at the sample surfaces. By explicitly calculating the surface contribution to the free energy

$$\Sigma=\lim_{L\to\infty}\frac{1}{L^2}\left[\Omega-L^3\left[\lim_{L\to\infty}\frac{\Omega}{L^3}\right]\right] \tag{3.33}$$

one can determine the most favorable number of layers n. Thus in general the grand canonical potential can be written as $\Omega=L^3\omega^{(b)}+L^2\Sigma+\cdots$. Note that there are finite size corrections to the coefficients of the equilibrium orientational distribution:

$$\mu_{lm}(\mathbf{r},L)=\mu^{(b)}_{lm}(\mathbf{r})+L^{-1}\mu^{(1)}_{lm}(\mathbf{r})+\cdots \tag{3.34}$$

so that the grand canonical potential becomes

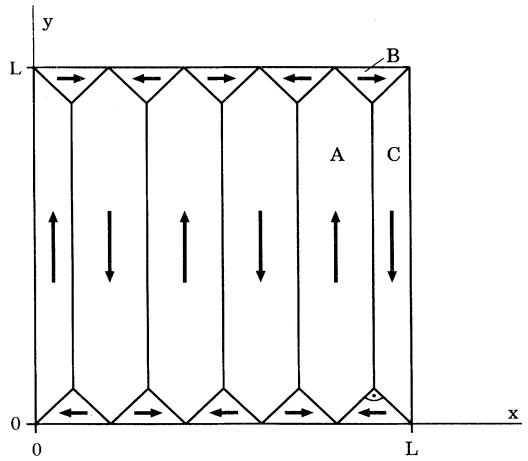

FIG. 8. The layered domain structure examined in Sec. III. Here the case $n=4$ is drawn; in general, the structure has n domains of type A, $2n+2$ domains of type B, and two domains of type C. The whole configuration is translational invariant in the z direction. Note that in order to ensure that the normal components of $\mathbf{M}$ are continuous at the domain boundaries the B domains must form angles of $\pi/2$ and $\pi/4$. The arrows indicate only the *mean value* of the orientation. However, in our calculation we consider a nontrivial orientational *distribution* $\alpha(\mathbf{r},\omega)$. Therefore we incorporate, within mean-field theory, fluctuations around the mean value $\mathbf{M}$.

$$\Omega(\{\mu_{lm}(\mathbf{r},L)\})=L^3\omega^{(b)}(\{\mu_{lm}^{(b)}(\mathbf{r})\}) + L^2\int d^3r\sum_{l,m}\mu_{lm}^{(1)}(\mathbf{r})\frac{\delta\omega^{(b)}}{\delta\mu_{lm}(\mathbf{r})}\bigg|_{\{\mu_{lm}^{(b)}(\mathbf{r})\}} + L^2\Sigma(\{\mu_{lm}^{(b)}(\mathbf{r})\})+\cdots . \quad (3.35)$$

But since by definition $[\delta\omega^{(b)}/\delta\mu_{lm}(\mathbf{r})]|_{\{\mu_{lm}^{(b)}(\mathbf{r})\}}=0$ the terms $\mu_{lm}^{(1)}(\mathbf{r})$ do not contribute to the surface free energy and will therefore be ignored in the following. There is no surface contribution to the entropic term given by Eq. (2.2), so that in Eq. (3.33) Ω can be replaced by $\Omega_{\rm int}$. According to Eq. (3.5) the interaction contribution to the grand canonical potential can be expressed as

$$\Omega_{\rm int}=-\frac{\rho^2}{2\beta}\sum_{i,j}\sum_{l_1,l_2,l}\sum_{m_1,m_2,m}C(l_1l_2l,m_1m_2m)\times\mu_{l_1m_1}^{(i)}\mu_{l_2m_2}^{(j)}I_{ij}^{l_1l_2lm} \quad (3.36)$$

with

$$I_{ij}^{l_1l_2lm}=\int_{V_i}d^3r\int_{V_j}d^3r'\hat{f}_{l_1l_2l}(r_{12})Y_{lm}(\omega_{12}) =(-1)^lI_{ji}^{l_1l_2lm} . \quad (3.37)$$

Here i and j denote the domains and the coefficients $\mu_{lm}^{(i)}$ parametrize the orientational distribution within the domain i according to Eq. (3.1). Since $I_{ij}^{l_1l_2lm}$ vanishes if l is odd [see Eq. (3.4)] the indices i and j can always be interchanged. Using the transformation $\mathbf{r}_S=\frac{1}{2}(\mathbf{r}+\mathbf{r}')$, $\mathbf{r}_{12}=\mathbf{r}-\mathbf{r}'$, one obtains

$$I_{ij}^{l_1l_2lm}=L^3\int_{V_{ij}}d^3r_{12}h_{ij}\left[\frac{\mathbf{r}_{12}}{L}\right]\hat{f}_{l_1l_2l}(r_{12})Y_{lm}(\omega_{12}) , \quad (3.38)$$

where

$$V_{ij}=\{\mathbf{r}_{12}\in\mathbb{R}^3|\mathbf{r}_{12}=\mathbf{r}-\mathbf{r}',\mathbf{r}\in V_i,\mathbf{r}'\in V_j\} \quad (3.39)$$

is the set of vector differences between points in domains i and j. One has $V_{ji}=-V_{ij}=\{\mathbf{r}\in\mathbb{R}^3|-\mathbf{r}\in V_{ij}\}$. The function $h_{ij}(\mathbf{r}_{12}/L)$ gives the volume of the set of possible vectors $\mathbf{r}_S$ for fixed $\mathbf{r}_{12}$ divided by the total volume L^3. It can be determined from the volume of the intersection of the sets V_i and V_j if they are displaced by the vector $\mathbf{r}_{12}$ relative to each other (see Fig. 9):

$$h_{ij}(\mathbf{r}_{12}/L)=L^{-3}\mathrm{vol}(\{\mathbf{r}'\in\mathbb{R}^3|\mathbf{r}'=\mathbf{r}-\mathbf{r}_{12},\mathbf{r}\in V_i\}\cap V_j) =h_{ji}(-\mathbf{r}_{12}/L) . \quad (3.40)$$

The functions $\hat{f}_{l_1l_2l}$ have the expansion $\hat{f}_{l_1l_2l}(r)=\sum_{k=3}^{\infty}c_k^{(l_1l_2l)}r^{-k}$ [which is valid for $r\geq\sigma$ (see Appendix B in Ref. [15])], where the long-ranged term with $k=3$ occurs only for $(l_1l_2l)=(112)$, whereas in all other cases the summation starts at $k=k_0\geq 6$. If the domains i and j are disjunct their minimal distance scales with the system size L [for an example see Fig. 9(c)] so that after the substitution $\mathbf{x}=\mathbf{r}_{12}/L$ Eq. (3.38) gives

$$I_{ij}^{l_1l_2lm}=\int d\omega\sum_{k=3}^{\infty}c_k^{(l_1l_2l)}L^{6-k}\times\int_{g_1(\omega)}^{g_2(\omega)}dx\,x^{2-k}h_{ij}(\mathbf{x})Y_{lm}(\omega) . \quad (3.41)$$

The definitions of $g_1(\omega)$ and $g_2(\omega)$ can be inferred from Fig. 9(c). The above expression does not contain any surface contributions $\sim L^2$ (there is a *bulk* contribution $\sim L^3$ from the long-ranged part of $\hat{f}_{112}$: $c_3^{(112)}\neq 0$ but $c_k^{(112)}=0$ for $k=4,\ldots,8$). If V_i and V_j are identical or have a common edge or surface the function h_{ij} can be expanded around $\mathbf{r}_{12}=\mathbf{0}$:

$$h_{ij}\left[\frac{\mathbf{r}_{12}}{L}\right]=\sum_{n=0}^{\infty}\left[\frac{r_{12}}{L}\right]^nh_{ij}^{(n)}(\omega_{12}) . \quad (3.42)$$

With $g(\omega)=r_{\max}(\omega)/L$ where $r_{\max}(\omega)$ defines the surface of V_{ij} (see Fig. 9) one has

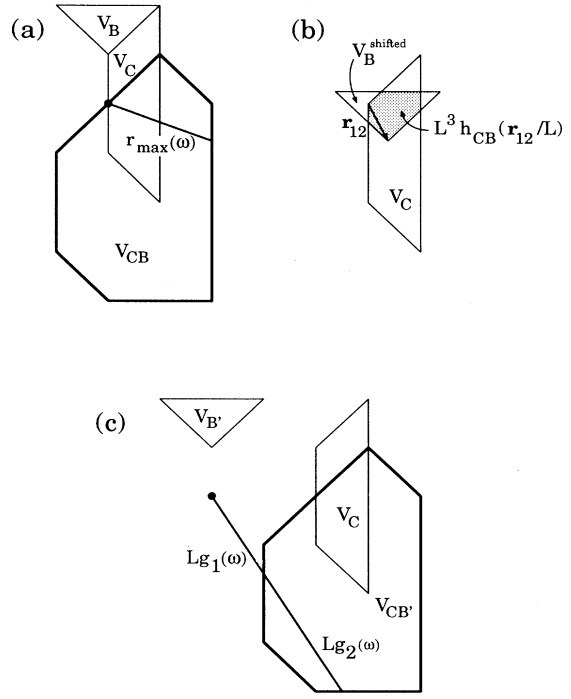

FIG. 9. (a) Construction of the integration volume for the integrals over $\mathbf{r}_{12}$ in Eq. (3.38) using a B and C domain as an example. The dot denotes the origin. The function $r_{\max}(\omega)$ defines the surface of the volume V_{CB}. Its height in the z direction is $2L$. (b) The function $L^3h_{BC}(\mathbf{r}_{12}/L)$ equals the shaded intersection volume of the C domain and the B domain which are translated by the vector $\mathbf{r}_{12}\in V_{CB}$ relative to each other [see Eq. (3.40)]. (c) The same construction as in (a) for two domains which have no common points. In this case the origin (dot) lies outside the integration volume $V_{CB'}$. The functions $Lg_1(\omega)$ and $Lg_2(\omega)$ define the lower and upper limits of the radial integral in the direction ω, respectively.

$$I_{ij}^{l_1 l_2 lm}=L^3\sum_{n=0}^{\infty}\sum_{k=3}^{\infty}\int d\omega\, h_{ij}^{(n)}(\omega)Y_{lm}(\omega)\times\int_{\sigma}^{Lg(\omega)}dr\, r^2 c_k^{(l_1 l_2 l)} r^{-k}\left[\frac{r}{L}\right]^n . \tag{3.43}$$

In accordance with Fig. 9 the angular integral over ω in Eq. (3.43) does not run over the whole unit sphere as long as the uniquely defined origin $\mathbf{r}_{12}=\mathbf{r}-\mathbf{r}'=\mathbf{0}$ does not lie within the interior of V_{ij}, i.e., for $i\neq j$. This is taken into account by putting $h_{ij}^{(n)}=0$ outside these accessible values of ω. The radial integral can be evaluated easily. Only the terms $\sim L^2$, i.e., $n=1$, contribute to Σ so that

$$\Sigma=-\frac{\rho^2}{2\beta}\sum_{i,j}{}'\sum_{l_1,l_2,l}\sum_{m_1,m_2,m}C(l_1 l_2 l,m_1 m_2 m)\mu_{l_1 m_1}^{(i)}\mu_{l_2 m_2}^{(j)}t_{l_1 l_2 l}\left[\frac{2l+1}{4\pi}\right]^{1/2}J_{ij}^{lm}$$
$$=\sum_{\Lambda}\Sigma^{(\Lambda)} , \tag{3.44}$$

where $\sum_{ij}'$ denotes the sum over neighboring domains i and j including $i=j$, $\Lambda=(l_1 l_2 l)$,

$$t_{l_1 l_2 l}=\sum_{k=3}^{\infty}\frac{1}{k-4}c_k^{(l_1 l_2 l)}\sigma^{4-k} , \tag{3.45}$$

and [see Eqs. (3.38) and (3.42)]

$$J_{ij}^{lm}=\left[\frac{4\pi}{2l+1}\right]^{1/2}\int d\omega\, h_{ij}^{(1)}(\omega)Y_{lm}(\omega)=(-1)^l J_{ji}^{lm} . \tag{3.46}$$

[In Eq. (3.45) the term $k=4$ does not pose a problem because according to the above discussion all coefficients $c_4^{(l_1 l_2 l)}$ vanish.] For $(l_1 l_2 l)\neq(112)$, $\hat{f}_{l_1 l_2 l}(r)$ decays as r^{-6} or faster so that

$$t_{l_1 l_2 l}=\int_{\sigma}^{\infty}dr\, r^3\hat{f}_{l_1 l_2 l}(r) , \tag{3.47}$$

but in the special case of the long-ranged coefficient $\hat{f}_{112}$ one finds [see Eq. (3.12)]

$$t_{112}=-(4\pi)^{3/2}\sqrt{\tfrac{2}{15}}\beta m^2\sigma+\int_{\sigma}^{\infty}dr\, r^3\hat{f}_{112}^{(\mathrm{SR})}(r) , \tag{3.48}$$

where

$$\hat{f}_{112}^{(\mathrm{SR})}=\hat{f}_{112}-\hat{f}_{112}^{(\mathrm{LR})}=\sum_{k=9}^{\infty}c_k^{(112)}r^{-k} .$$

Note that $t_{l_1 l_2 l}$ is zero unless both l_1+l_2 and l are even [see Eq. (3.4)].

In the domain structure under consideration (see Fig. 8) there are n hexagonal domains, which we will call type A, $2n+2$ triangular domains (type B), and two trapezoidal domains (type C). Since $h_{ij}^{(1)}(\omega)$ is zero if the domains i and j have only a common edge (like two neighboring triangular domains), only combinations of a domain with itself or with a domain with a common face have to be taken into account. Since l is even the integral $I_{ij}^{l_1 l_2 m}$ in Eq. (3.37) is invariant under simultaneous translations of both domains or inversions at any point. Reflection of both domains at the xz plane leads to the complex conjugated integral since $Y_{lm}(\theta,-\phi)=Y_{lm}^*(\theta,\phi)$. Due to these symmetries the actual calculation is reduced to seven cases: the combination of a domain with itself for all three types ($J_{AA}^{lm}, J_{BB}^{lm}, J_{CC}^{lm}$), domains A or C with a domain B attached at the upper left boundary (J_{AB}^{lm}, J_{CB}^{lm}), two adjoining domains A with A' to the left of A ($J_{AA'}^{lm}$), and a domain A in contact with a domain C to its left (J_{AC}^{lm}). For these cases the functions $h_{ij}^{(1)}$ are obtained by determining the overlap volume of the translated domains [see Eq. (3.40) and Fig. 9]. For example, one finds

$$h_{AA}^{(1)}(\theta,\phi)=\begin{cases}-|\cos\phi|\sin\theta-|\cos\theta|\dfrac{1+2n}{2(1+n)^2}, & -\dfrac{\pi}{4}\le\phi\le\dfrac{\pi}{4}\ \text{ or }\ \dfrac{3\pi}{4}\le\phi\le\dfrac{5\pi}{4}\\ -\dfrac{n|\cos\phi|+|\sin\phi|}{1+n}\sin\theta-|\cos\theta|\dfrac{1+2n}{2(1+n)^2}, & \dfrac{\pi}{4}\le\phi\le\dfrac{3\pi}{4}\ \text{ or }\ -\dfrac{\pi}{4}\ge\phi\ge-\dfrac{3\pi}{4}\end{cases} \tag{3.49}$$

and

$$h_{AA'}^{(1)}(\theta,\phi)=h_{AC}^{(1)}(\theta,\phi)=\begin{cases}\dfrac{n}{n+1}\cos\phi\sin\theta, & -\dfrac{\pi}{2}\le\phi\le\dfrac{\pi}{2}\\ 0\ \text{ otherwise} .\end{cases} \tag{3.50}$$

We are now in the position to compute the surface contribution to the free energy $\Sigma=\sum_{\Lambda}\Sigma^{(\Lambda)}$ which, in principle, is an infinite sum. However, we constrain our analysis to the most important contributions. This approach is reasonable because Σ is already overestimated by assuming sharp domain boundaries; therefore it is appropriate to refrain from computing this approximate expression

for Σ [Eq. (3.44)] with high precision. This additional approximation is justified as long as it does not prohibit one from predicting correctly which of the considered configurations is, within the same approximation scheme, the most favorable one. Guided by the experience [8] that in a needle-shaped volume the equilibrium orientational distribution is dominated, at least close to the phase transition to the isotropic liquid, by the terms $l=0$ and 1 in Eq. (3.1), we assume $l_1,l_2\in\{0,1\}$. Since l_1+l_2 must be even and due to the selection rule for the Clebsch-Gordan coefficients (see Appendix B in Ref. [15]) this implies that we have to consider three terms in Σ:

$$\Sigma=\Sigma^{(000)}+\Sigma^{(110)}+\Sigma^{(112)}+\cdots . \tag{3.51}$$

$\Sigma^{(000)}$ is the surface contribution which arises from the isotropic configuration $\mu_{lm}=(1/\sqrt{4\pi})\delta_{l,0}$. Since the value of μ_{00} is fixed by the normalization, $\Sigma^{(000)}$ is the same for all configurations, independent of the domain structure. For an isotropic fluid in a cube as considered here one has $\Sigma^{(000)}=6\sigma^{\rm iso}_{f,{\rm vac}}$ where $\sigma^{\rm iso}_{f,{\rm vac}}$ is the surface tension between the isotropic fluid and vacuum. If the fluid is magnetized, $\frac{1}{6}\Sigma^{(000)}$ corresponds to the magnetization-independent contribution to the anisotropic fluid-vacuum interface tension [see Eq. (3.72)]. Within the approach explained above the domains shown in Fig. 8 are specified by the coefficients $\mu^{(i)}_{lm}$. Since the magnetization lies in the xy plane everywhere one has $\mu^{(i)}_{10}=0$ [see Eq. (3.15)]. For the domains of type A and C one has $\mu_{11}=\pm Ai$ and $\mu_{11}=\pm A$ for the domains of type B where $A=\sqrt{(3/8\pi)}(|\mathbf{M}|/m\rho)$. According to Fig. 8 the signs alternate from domain to domain. This implies that we have to determine the quantities J^{lm}_{ij} for $(l,m)=(0,0)$, (2,0), and (2,2); (2,1) does not occur because $m=m_1+m_2$ and $m_1,m_2=\pm1$. Furthermore, we have $J^{lm}_{ij}=J^{lm}_{ji}$ since l is even and $J^{l\bar{m}}_{ij}=(J^{lm}_{ij})^*$. Using MATHEMATICA we find

$$J^{00}_{AA}=-\pi\frac{1+2\sqrt{2}+4n+2\sqrt{2}n+2n^2}{(1+n)^2} ,$$
$$J^{20}_{AA}=-\pi\frac{1-\sqrt{2}+n-\sqrt{2}n-n^2}{4(1+n)^2} , \tag{3.52}$$
$$J^{22}_{AA}=-\pi\frac{\sqrt{6}n}{8(1+n)} , \quad J^{00}_{BB}=-\pi\frac{3+2\sqrt{2}+2n+2\sqrt{2}n}{2(1+n)^2} , \tag{3.53}$$
$$J^{20}_{BB}=\pi\frac{\sqrt{2}+n+\sqrt{2}n}{8(1+n)^2} , \quad J^{22}_{BB}=\pi\frac{\sqrt{6}}{16(1+n)} , \tag{3.54}$$
$$J^{00}_{CC}=-\pi\frac{3+2\sqrt{2}+8n+2\sqrt{2}n+4n^2}{2(1+n)^2} ,$$
$$J^{20}_{CC}=\pi\frac{\sqrt{2}+n+\sqrt{2}n+2n^2}{8(1+n)^2} , \tag{3.55}$$
$$J^{22}_{CC}=-\pi\frac{\sqrt{6}(1+2n)}{16(1+n)} , \tag{3.56}$$
$$J^{00}_{AC}=\pi\frac{n}{1+n} , \quad J^{20}_{AC}=-\pi\frac{n}{8(1+n)} , \quad J^{22}_{AC}=\pi\frac{\sqrt{6}n}{16(1+n)} , \tag{3.57}$$
$$J^{00}_{AB}=\pi\frac{\sqrt{2}}{2(1+n)} , \quad J^{20}_{AB}=-\pi\frac{\sqrt{2}}{16(1+n)} ,$$
$$J^{22}_{AB}=-i\pi\frac{\sqrt{3}}{16(1+n)} , \tag{3.58}$$

and $J^{lm}_{AA'}=J^{lm}_{AC}$, $J^{lm}_{CB}=J^{lm}_{AB}$. This finally leads to the following terms in the surface contribution to the free energy [see Eq. (3.44)]:

$$\Sigma^{(000)}=\frac{3}{8\sqrt{\pi}}\frac{\rho^2}{\beta}t_{000} , \tag{3.59}$$

$$\Sigma^{(110)}=-\frac{1}{4\sqrt{3\pi}}\frac{\rho^2}{\beta}t_{110}A^2[-nJ^{00}_{AA}-2J^{00}_{CC}-2(n+1)J^{00}_{BB}+2(n-1)J^{00}_{AA'}+4J^{00}_{AC}]$$
$$=-\left[\frac{\pi}{3}\right]^{1/2}\frac{\rho^2}{\beta}t_{110}A^2(2n+3+2\sqrt{2}) , \tag{3.60}$$

and

$$\Sigma^{(112)}=-\left[\frac{5}{4\pi}\right]^{1/2}\frac{\rho^2}{\beta}t_{112}A^2\left[-n\,{\rm Re}J^{22}_{AA}-2\,{\rm Re}J^{22}_{CC}+2(n+1){\rm Re}J^{22}_{BB}+2(n-1){\rm Re}J^{22}_{AA'}+4\,{\rm Re}J^{22}_{AC}\right.$$
$$\left.-8n\,{\rm Im}J^{22}_{AB}-8\,{\rm Im}J^{22}_{CB}+\frac{1}{\sqrt{6}}\{-nJ^{20}_{AA}-2J^{20}_{CC}-2(n+1)J^{20}_{BB}+2(n-1)J^{20}_{AA'}+4J^{20}_{AC}\}\right]$$
$$=-\frac{1}{4}\left[\frac{5\pi}{6}\right]^{1/2}\frac{\rho^2}{\beta}t_{112}A^2(2n+3+2\sqrt{2}) . \tag{3.61}$$

It is a very useful and nontrivial check to see that $\frac{1}{6}\Sigma^{(000)}=\sigma^{\rm iso}_{f,{\rm vac}}$ coincides with the corresponding expression given before Eq. (4.33) in Ref. [15]. Although the above derivation cannot be applied to the special case $n=0$, which corresponds to the triangular structure with four domains as shown in Fig. 10, an analogous analysis for this configuration shows that the final results in Eqs. (3.59)–(3.61) remain nonetheless valid for $n=0$. With

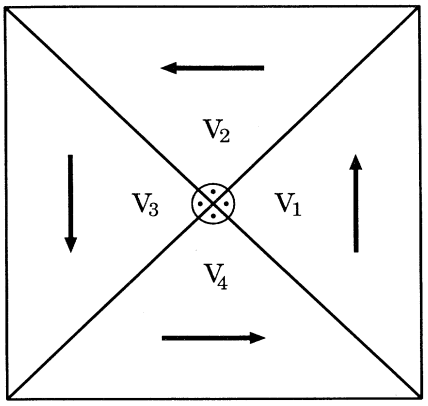

FIG. 10. The triangular domain structure in a cube exhibits the lowest surface energy of all considered configurations with sharp domain boundaries. The last part of the caption of Fig. 9 applies here, too.

the expressions for the functions $\hat{f}_{110}(r)$ and $\hat{f}_{112}(r)$ given by Eqs. (B33) and (B34) in Ref. [15] we find

$$t_{110}=-\frac{8\pi}{25}\left[\frac{4\pi}{3}\right]^{1/2}\beta^3 m^6\int_\sigma^\infty dr\, r^{-6}e^{-\beta w_{\mathrm{LJ}}(r)} +O(m^{10}) \tag{3.62}$$

and

$$t_{112}=(4\pi)^{3/2}\sqrt{\tfrac{2}{15}}\beta m^2\left[-\sigma+\int_\sigma^\infty dr\,(e^{-\beta w_{\mathrm{LJ}}(r)}-1)\right] +O(m^6)\ . \tag{3.63}$$

Therefore for small m $\Sigma-\Sigma^{(000)}$ is dominated by $\Sigma^{(112)}$. Since t_{112} is negative for $T^*>0.717$, Eq. (3.61) implies that Σ is minimal for $n=0$. We do not consider the case $T^*<0.717$ because at such low temperatures one encounters freezing which is not captured by the present approach. Thus we conclude that the configuration in Fig. 10 is the most favorable one among those considered. Although in the actual equilibrium configuration the sharp domain boundaries will be replaced by a smooth variation of the magnetization, the above result indicates that "large-scale" structures with only very few rotations of **M** upon traversing the sample are favored.

C. Surface tension between domains

In the following we show that the results in Eqs. (3.60) and (3.61) can also be obtained by adding the surface tensions of the individual domain boundaries. This demonstrates that in the thermodynamic limit the various domain walls do not exhibit an effective interaction between them, which would preclude this linear superposition. In order to be able to extract one single surface tension from the total surface contribution to the free energy first a homogeneously magnetized cuboid with side lengths $l_i L\,(i=x,y,z)$ is examined. In analogy to the above calculation we find

$$\Sigma_{\mathrm{hom}}=-\frac{\rho^2}{2\beta}\sum_{l_1,l_2,l}\sum_{m_1,m_2,m}C(l_1l_2l,m_1m_2m) \times\mu_{l_1m_1}\mu_{l_2m_2}t_{l_1l_2l} \times\left[\frac{2l+1}{4\pi}\right]^{1/2}J^{lm} \tag{3.64}$$

with

$$J^{lm}=\left[\frac{4\pi}{2l+1}\right]^{1/2}\int d\omega\, h^{(1)}(\omega)Y_{lm}(\omega)\ . \tag{3.65}$$

In this case the function h defined by Eq. (3.40) with $V_i=V_j=V$ is

$$h(x,y,z)=(l_x-|x|)(l_y-|y|)(l_z-|z|) \tag{3.66}$$

so that

$$h^{(1)}(\theta,\phi)=-l_yl_z|\cos\phi|\sin\theta-l_xl_z|\sin\phi|\sin\theta -l_xl_y|\cos\theta|\ , \tag{3.67}$$

which gives

$$J^{00}=-2\pi(l_yl_z+l_xl_z+l_xl_y)\ ,$$
$$J^{20}=\frac{\pi}{4}(l_yl_z+l_xl_z-2l_xl_y)\ , \tag{3.68}$$
$$J^{22}=\frac{\pi}{4}\sqrt{\tfrac{3}{2}}(-l_yl_z+l_xl_z)\ .$$

If the magnetization lies in the xy plane and is given by $\mu_{11}=-Ae^{-i\phi}$ the evaluation of Eq. (3.64) yields

$$\Sigma_{\mathrm{hom}}^{(000)}=\frac{1}{8\sqrt{\pi}}\frac{\rho^2}{\beta}t_{000}(l_yl_z+l_xl_z+l_xl_y)\ , \tag{3.69}$$

$$\Sigma_{\mathrm{hom}}^{(110)}=-\left[\frac{\pi}{3}\right]^{1/2}\frac{\rho^2}{\beta}t_{110}A^2(l_yl_z+l_xl_z+l_xl_y)\ , \tag{3.70}$$

and

$$\Sigma_{\mathrm{hom}}^{(112)}=-\frac{1}{8}\left[\frac{5\pi}{6}\right]^{1/2}\frac{\rho^2}{\beta}t_{112}A^2 \times[3\cos2\phi(-l_yl_z+l_xl_z) -(l_yl_z+l_xl_z-2l_xl_y)]\ . \tag{3.71}$$

Due to the explicit dependences on the side lengths the different terms can now be assigned to the individual faces of the cuboid. Thus the surface tension $\sigma_{f,\mathrm{vac}}(\phi)$ between vacuum and a half space magnetized in a direction forming an angle ϕ with the surface normal is

$$\sigma_{f,\mathrm{vac}}(\phi)=\sum_{l_1,l_2,l}\sigma_{f,\mathrm{vac}}^{(l_1l_2l)} \tag{3.72}$$

with

$$\sigma_{f,\mathrm{vac}}^{(000)}=\frac{1}{16\sqrt{\pi}}\frac{\rho^2}{\beta}t_{000}\ , \tag{3.73}$$

$$\sigma_{r,\mathrm{vac}}^{(110)}=-\frac{1}{2}\left[\frac{\pi}{3}\right]^{1/2}\frac{\rho^2}{\beta}t_{110}A^2\ , \tag{3.74}$$

$$\sigma_{f,\mathrm{vac}}^{(112)}=\frac{1}{16}\left[\frac{5\pi}{6}\right]^{1/2}\frac{\rho^2}{\beta}t_{112}A^2[3\cos2\phi+1]\ . \tag{3.75}$$

By using Eq. (3.63) one sees that the surface tension with the vacuum is maximal (minimal) if the magnetization is tangential (orthogonal) to the interface.

Now we consider two adjacent cubes of side length L which touch each other in the xz plane. The magnetization in both cubes is taken to lie in the xy plane, having the same angle α with the interface normal, i.e., the y axis. (Thus the normal component of $\mathbf{M}$ is continuous at the interface in order to avoid magnetic surface charges and the parallel components point in opposite directions.) With the same method as described above the surface contribution to the free energy is found to be

$$\Sigma^{(000)}=\frac{5}{4\sqrt{\pi}}\frac{\rho^2}{\beta}t_{000}\ , \tag{3.76}$$

$$\Sigma^{(110)}=-\left[\frac{\pi}{3}\right]^{1/2}\rho\frac{2}{\beta}t_{110}A^2(-\cos2\alpha+6)\ , \tag{3.77}$$

$$\Sigma^{(112)}=-\frac{1}{8}\left[\frac{5\pi}{6}\right]^{1/2}\frac{\rho^2}{\beta}t_{112}A^2(\cos2\alpha+3)\ . \tag{3.78}$$

By subtracting the appropriate vacuum surface tensions at the outer surfaces one obtains for the surface tension between the two domains

$$\sigma_{f,f}=\sum_{l_1,l_2,l}\sigma_{f,f}^{(l_1l_2l)} \tag{3.79}$$

with

$$\sigma_{f,f}^{(000)}=0\ , \tag{3.80}$$

$$\sigma_{f,f}^{(110)}=-\left[\frac{\pi}{3}\right]^{1/2}\frac{\rho^2}{\beta}t_{110}A^2[1-\cos2\alpha]\ , \tag{3.81}$$

$$\sigma_{f,f}^{(112)}=-\frac{1}{4}\left[\frac{5\pi}{6}\right]^{1/2}\frac{\rho^2}{\beta}t_{112}A^2[1-\cos2\alpha]\ . \tag{3.82}$$

This surface tension vanishes if the two domains are magnetized in the same direction (i.e., $\alpha=0$) and is maximal when they are magnetized in opposite directions (i.e., $\alpha=\pi/2$). Adding the contributions from the individual interfaces of the assumed domain structure (Fig. 8) and taking into account the angles between the magnetization vectors as well as the interface areas leads to the same result for the total surface contribution to the free energy as the direct calculation. We conjecture that this additivity is valid in general. This would mean that among the configurations with sharp domain boundaries one could minimize the total surface contribution to the free energy by looking for structures with small interface areas and small changes of the direction of the magnetization between adjacent domains. In this sense most probably the triangular structure is already the optimum for a cube. Of course we expect that the surface contribution to the free energy can be lowered even further by introducing broadened domain walls. This substantially more difficult problem is left to a further study. Nonetheless, the present analysis provides already a rough picture of what the actual equilibrium configuration presumably looks like.

IV. DOMAIN STRUCTURES AND PHASE DIAGRAMS IN EXTERNAL FIELDS

A sufficiently large external field will destroy any domain structure since it favors the orientation of all dipoles parallel to the field. Small fields, however, cause only small perturbations of the zero field structure. Thus there is a phase transition between an inhomogeneously and a homogeneously magnetized phase at a critical value of the external field [12,13]. Here we study the case where in the zero field configuration the magnetization is confined to the xy plane. The external field $\mathbf{H}=H\mathbf{e}_z$ induces an additional z component of the magnetization, which is spatially constant due to the symmetry, and also changes the values of the spatially inhomogeneous x and y components. As a specific example one may think of the triangular configuration in a cube (see Fig. 10), but the following discussion holds for *all* zero field domain structures with $M_z=0$ and $\mathbf{H}_d=\mathbf{0}$ in any sample shape.

If for finite but not too large external fields $\mathbf{H}$ and $\mathbf{M}$ are not collinear one can surmise that the orientational distribution is no longer axially symmetric. But deviations from the axial symmetry can occur only in the terms with $l\geq2$ in Eq. (3.1) because the $l=0$ term is fixed by the normalization and the $l=1$ terms are fully determined by the magnetization $\mathbf{M}(\mathbf{r})$ [see Eq. (3.15)]. Thus we expect that this possible anisotropy is only a small effect and therefore it is ignored in the following analysis, which reduces the number of parameters for the minimization of the free energy. (Indeed a numerical minimization taking into account *all* μ_{lm} up to $l=2$ indicates that even in this approximation the equilibrium orientational distribution remains axially symmetric.) So we focus our analysis on configurations $\alpha(\mathbf{r},\omega)$ that emerge from a single axially symmetric configuration

$$\tilde{\alpha}(\cos\theta)=\frac{1}{2\pi}\sum_{l=0}^{\infty}\alpha_lP_l(\cos\theta) \tag{4.1}$$

by applying local rotations. The coefficients α_l are spatially constant. As shown in Sec. III the entropic term is given as

$$S=2\pi\int_{-1}^{1}dx\ \tilde{\alpha}(x)\ln[4\pi\tilde{\alpha}(x)] \tag{4.2}$$

and the bulk contribution of the short-ranged part of the interaction contribution is given as [see Eqs. (3.10) and (3.11)]

$$\lim_{V\to\infty}\frac{\Omega_{\mathrm{int}}^{(\mathrm{SR})}}{V}=\rho^2\sum_{l=0}^{\infty}\hat{u}_l\alpha_l^2\ , \tag{4.3}$$

so that both are independent of the spatial variation of the orientation of $\mathbf{M}(\mathbf{r})$. However, the field energy cannot be expressed solely in terms of the coefficients $\{\alpha_l\}$. With $|\mathbf{M}|=\frac{2}{3}\rho m\alpha_1$, Eq. (3.15), and due to the fact that M_z is constant, one has

$$\frac{\Omega_H}{V}=-\left[\frac{4\pi}{3}\right]^{1/2}\rho m H\mu_{10}=-\tfrac{2}{3}\rho m H\alpha_1\cos\theta_M\ , \qquad (4.4)$$

where θ_M denotes the angle between $\mathbf{M}(\mathbf{r})$ and $\mathbf{H}$, which in the present case is constant. Consequently the configuration is completely described by the coefficients $\{\alpha_l\}$ and θ_M. The grand canonical potential must be minimized with respect to them.

Despite $\nabla\cdot\mathbf{M}=0$ the demagnetization field for such configurations is no longer zero since the z component of the magnetization leads to a magnetic surface charge density on the upper and lower surfaces of the sample. The first line of Eq. (3.20) shows that for the configurations under consideration $\mathbf{H}_d$ is the same as for a configuration with $\mathbf{M}=(0,0,M_z)$. Since M_z is a constant throughout the sample, Eq. (3.26) applies, which leads to

$$1/(8\pi)\int_{\mathbb{R}^3}d^3r\,\mathbf{H}_d^2(\mathbf{r})=2\pi V D_{33}M_z^2\ .$$

Thus with Eq. (3.25) one finds

$$\lim_{V\to\infty}\frac{\Omega_{\rm int}^{(\rm LR)}}{V}=2\pi D_{33}M_z^2-\frac{2\pi}{3}\mathbf{M}^2$$
$$=-\frac{8\pi}{27}\rho^2m^2\alpha_1^2(1-3D_{33}\cos^2\theta_M)\ . \qquad (4.5)$$

(Since in general one has $\sum_i D_{ii}=1$ [19] a symmetry argument gives $D_{33}=\frac{1}{3}$ for a cube.) To summarize, the bulk contribution to the density functional for the configurations under consideration reduces to

$$\lim_{V\to\infty}\frac{\Omega}{V}=f_{\rm HS}(\rho)+2\pi\frac{\rho}{\beta}\int_{-1}^{1}dx\,\tilde\alpha(x)\ln[4\pi\tilde\alpha(x)]$$
$$+\rho^2\sum_{l=0}^{\infty}\hat u_l\alpha_l^2-\frac{8\pi}{27}\rho^2m^2\alpha_1^2(1-3D_{33}\cos^2\theta_M)$$
$$-\tfrac{2}{3}\rho m H\alpha_1\cos\theta_M-\mu\rho\ . \qquad (4.6)$$

In order to determine the equilibrium configuration this expression is minimized with respect to $\cos\theta_M$ and $\tilde\alpha(x)$ which yields

$$\frac{8\pi}{3}D_{33}\rho m\alpha_1\cos\theta_M-H=0 \qquad (4.7)$$

and

$$\tilde\alpha(x)=\frac{1}{2\pi}\frac{f(x)}{\int_{-1}^{1}dx\,f(x)} \qquad (4.8)$$

with

$$f(x)=\exp\left[-\beta\rho\sum_{l=1}^{\infty}(2l+1)\hat u_l\alpha_l P_l(x)+\beta mH(\cos\theta_M)x\right.$$
$$\left.+\frac{8\pi}{9}\beta\rho m^2\alpha_1(1-3D_{33}\cos^2\theta_M)x\right]\ . \qquad (4.9)$$

The ansatz $\tilde\alpha(x)=(C/2\pi)\exp[\sum_{l=1}^{\infty}\gamma_l P_l(x)]$ leads to a system of equations consisting of Eq. (2.13) (where [see Eq. (3.11)] $u_l=\hat u_l$ for $l\geq 2$) and

$$\gamma_l=\left[-\frac{9}{2}\beta\rho\hat u_1+\frac{4\pi}{3}\beta\rho m^2(1-3D_{33}\cos^2\theta_M)\right]C$$
$$\times\int_{-1}^{1}dx\,x\exp\left[\sum_{l=1}^{\infty}\gamma_l P_l(x)\right]+\beta mH\cos\theta_M\ . \qquad (4.10)$$

By solving these equations numerically one finds that for small fields, high densities, or at low temperatures the fluid is in the domain phase, i.e., $\cos\theta_M<1$, while for large fields, low densities, or at high temperatures the fluid is homogeneously magnetized with $\cos\theta_M=1$. In the latter case the stationarity condition Eq. (4.7) is not necessarily satisfied because the global minimum at $\cos\theta_M=1$ lies on the boundary of the allowed region for the variational parameter $\cos\theta_M$.

As already pointed out in Sec. III the spatial distribution of the domains is not determined by the bulk contribution to the free energy but by the surface and line contributions. However, it is very probable that the actual configuration for $H\neq 0$ is a gentle distortion of the optimal configuration in zero field. Within our approach for a cubic sample this is given by Fig. 10 with the magnetization tilted out of plane within each domain towards the field direction, which is orthogonal to the plane.

Figure 11 displays the behavior of the magnetization at fixed density and temperature for a cube, i.e., $D_{33}=\frac{1}{3}$. At low fields the parallel component $M_\parallel=M_z=\frac{2}{3}\rho m\alpha_1\cos\theta_M$ increases linearly with the field [see Eq. (4.7)] while the perpendicular component $M_\perp=\frac{2}{3}\rho m\alpha_1\sin\theta_M$ decreases and vanishes at the critical field H_c. At higher fields M_z saturates. The temperature dependence at fixed field and density is shown in Fig. 12.

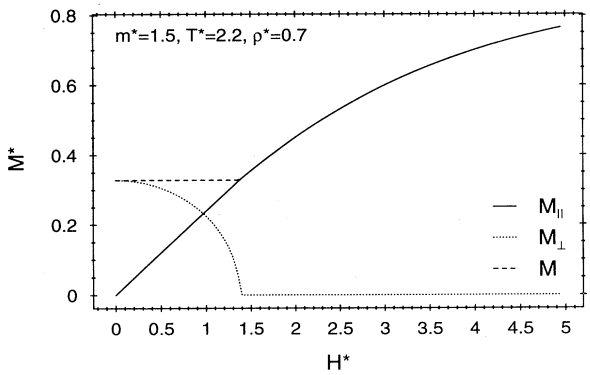

FIG. 11. Magnetization components parallel ($M_\parallel$, solid line) and perpendicular ($M_\perp$, dotted line) to the external field as a function of the strength of this field in a cubic sample. At low fields the parallel component increases strictly linearly [Eq. (4.7)] whereas the perpendicular component decreases and vanishes $\sim(H_c-H)^{1/2}$ at a critical field H_c. Above this field the sample is homogeneously magnetized. Equation (4.7) holds for $0\leq H\leq H_c$ whereas it is no longer valid for $H>H_c$ where $\theta_M=0$ independent of H. $M=(M_\parallel^2+M_\perp^2)^{1/2}=M_\perp$ for $H\geq H_c$.

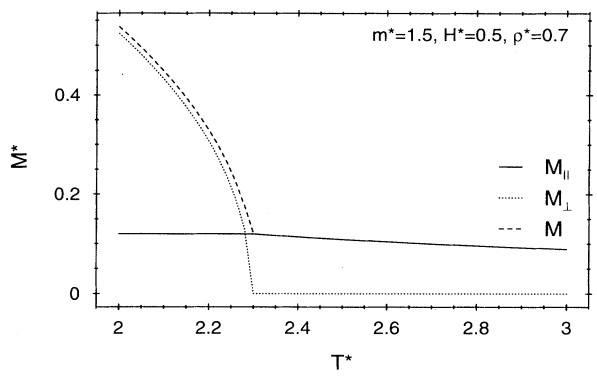

FIG. 12. Dependence of the magnetization components on the temperature at constant external field. At the transition temperature T_c between the domain phase ($T<T_c$) and the homogeneous phase ($T>T_c$) the component $M_{\parallel}$ parallel to the field exhibits a kink. In accordance with Eq. (4.7) $M_{\parallel}$ is constant for $\theta_M \neq 0$, i.e., for $T \leq T_c$. For $T>T_c$ $M=M_{\parallel}$.

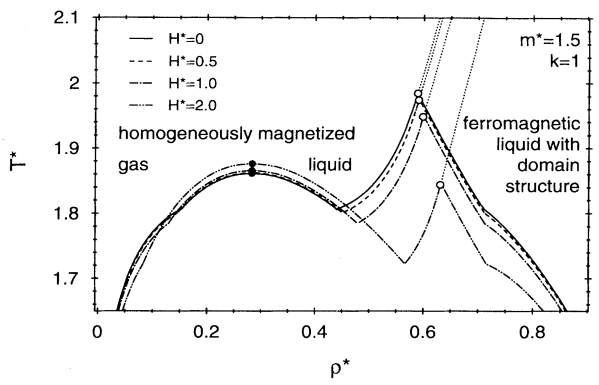

FIG. 13. Phase diagrams for a cubic sample for different constant values of the external field H. In contrast to the case of a long needle (see Fig. 3) the tricritical point (open circles) and the line of second order transitions (dotted liens) remain at finite fields. As a function of H the value of T_c (full circles) increases whereas the value of the tricritical temperature decreases. The magnetic field shifts the phase transition between the homogeneously magnetized fluid and the fluid with domain structure towards higher densities. Below the tricritical point this transition is first order. For $H=0$ the phase diagram is the same as in Fig. 2 for $H=0$.

The parallel component is constant in the domain phase [see Eq. (4.7)] and exhibits a kink at the critical point. For solid dipolar ferromagnets this kink has been predicted by Wojtowicz and Rayl [13] and experimentally observed by Frowein and Kötzler [20]. The above results are in accordance with the discussion of a dipolar ferromagnet in a torus in Ref. [13]. We emphasize the fact that due to the domain formation, which is a consequence of the long-ranged nature of the dipolar forces, a second order phase transition occurs also in the presence of an external field. As long as the phase transition is continuous the surface of critical points $\rho_c(T,H)$ is given by [see Eq. (4.7)]

$$\frac{8\pi}{9}\rho_c m \alpha_{1,c}(\rho_c,T,H)=H \ , \tag{4.11}$$

where

$$\alpha_{1,c}(\rho_c,T,H)=[-\gamma_1(T,H)+\beta m H]/(3\beta\rho_c \hat{u}_1)$$

is defined by the solution of Eqs. (2.13) and (4.10) for $\cos\theta_M=1$ [compare Eq. (4.23) in Ref. [8]].

Phase diagrams are calculated along the same lines as in Sec. II and displayed in Fig. 13. They strongly resemble the zero field phase diagram with a tricritical point and a first order phase transition below this point. With increasing field strength the line of second order transitions and the tricritical point are shifted to higher densities and lower temperatures. The overall influence of the field is much smaller than in the case of the needle-shaped sample (compare the curves for $H^*=0.5$ in Figs. 2 and 13). Thus we find that for nonzero external fields the bulk free energy and the phase diagrams depend on the sample shape via the demagnetization factor D_{33} in Eqs. (4.5), (4.6), and (4.10). However, Eq. (4.7) implies that for $H \to 0$ one has $\cos\theta_M \to 0$ (or $\alpha_1 \to 0$) so that the dependence on D_{33} drops out, rendering a shape-independent free energy in agreement with Griffiths's theorem. If one increases the aspect ratio k, i.e., decreases D_{33}, for fixed H the line of continuous phase transitions in Fig. 13 shifts to ever higher densities. Simultaneously a second critical point evolves at medium densities (see Fig. 14 where $D_{33}=0.010\,75$) so that in the limit $k \to \infty$ one arrives at the phase diagrams shown in Fig. 2.

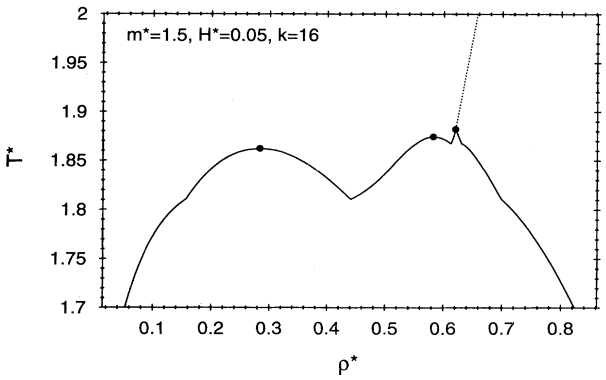

FIG. 14. Phase diagram for $m^*=1.5$, $H^*=0.05$, and a sample shape which has the same demagnetization factor as an ellipsoid with aspect ratio $k=16$ (i.e., $D_{33}=0.101\,75$). Compared with the case $k=1$ (see Fig. 13) the line of critical points is shifted to higher densities, the tricritical temperature is decreased, and a second critical point has emerged at medium densities, so that there are two triple points at $T^*=1.811$ and 1.867, respectively, at each of which three fluid phases coexist. At even higher aspect ratios the tricritical point turns into a critical end point and the line of critical points moves to even higher densities. In the limit $k \to \infty$ one recovers the phase diagram shown in Fig. 2.

V. STRIPES AND BUBBLES

Recently domain formation in a wide variety of physical systems has attracted considerable interest [14]. As examples we mention Langmuir films (i.e., monolayers of surfactants at fluid surfaces) of dipolar molecules [21] and thin films of uniaxial ferromagnets [22]. In these and many other systems a striped domain phase and a phase of "bubble" domains forming a periodic hexagonal superstructure can be observed. Figure 2 in Ref. [14] shows these structures in a phase-separated binary system consisting of a ferrofluid and a nonmagnetic fluid confined between parallel plates with a strong magnetic field perpendicular to the plates. In the ferrofluid all particles are aligned parallel to the field and the domain structure is only produced by the presence of the second fluid. These systems differ from the one-phase ferrofluid in weak or zero field which is discussed here in so far as they can be described by one-component order parameters. Nevertheless, in this section we will analyze the possibility of stripe and bubble phases in dipolar fluids in the framework of our approach. The only reported domain structure for these fluids found in simulations (see Fig. 12 in Ref. [2]) approximately corresponds to the stripe phase, but in this case the periodicity is induced by the periodic boundary conditions. Note that these configurations do not belong to the class described in Sec. III because the magnetization is not everywhere tangential to the surface. Nevertheless, as will be shown below, the demagnetization energy can be made negligibly small if the domain size is small compared to the system size.

A. Stripes

For the stripe phase we make the ansatz

$$\alpha(\mathbf{r},\omega)=\sum_{q}\sum_{l,m}a_{qlm}e^{iqy}Y_{lm}(\omega)\ , \tag{5.1}$$

where the y direction is perpendicular to the plane of the stripes. q takes on the values $0,\pm q_0,\pm 2q_0,\ldots$ where $q_0=\pi/D$ is the fundamental wave number corresponding to the width D of the stripes. Since α is real and normalized the coefficients a_{qlm} fulfill the relations

$$a_{qlm}=(-1)^m a^*_{-ql\bar{m}},\quad a_{q00}=\frac{1}{\sqrt{4\pi}}\delta_{q,0}. \tag{5.2}$$

Note that in contrast to Secs. III and IV here the domain walls are not sharp but smooth. The local magnetization is given by Eq. (3.15) with

$$\mu_{lm}(y)=\sum_{q}e^{iqy}a_{qlm}\ . \tag{5.3}$$

From macroscopic considerations [see the discussion after Eq. (5.30)] one expects that for large system sizes the number of domains increases as L^{ν} with $0<\nu<1$. Therefore the domain width increases as $L^{1-\nu}$ so that q_0 varies $\sim L^{\nu-1}$. According to Ref. [22] a single mode dominates near the transition to the homogeneous phase. For this reason we confine our analysis to the case that in Eq. (5.1) q takes on only the values $-q_0$, 0, and q_0 (with $q_0>0$). When Eq. (5.1) is inserted into Eq. (2.3) a lengthy calculation yields the following expression for the interaction contribution for a cubic sample:

$$\Omega_{\rm int}=\Omega_{\rm int}^{(\rm SR)}+\Omega_{\rm int}^{(\rm LR)}\ , \tag{5.4}$$

with

$$\begin{aligned}\frac{\Omega_{\rm int}^{(\rm SR)}}{V}=\pi\rho^2\Bigg\{&\sum_{l}(2l+1)\hat{u}_l\sum_{m}\Bigg[|a_{0lm}|^2+2|a_{q_0lm}|^2+\frac{\sin q_0L}{q_0L}2\,\mathrm{Re}(a_{q_0lm}a^*_{-q_0lm})\\&+\frac{\sin(q_0L/2)}{q_0L/2}4\,\mathrm{Re}(a_{q_0lm}a^*_{0lm})\Bigg]-\frac{1}{3}q_0^2\sum_{l}v_l\sum_{m}|a_{q_0lm}|^2\\&+\frac{1}{15}q_0^2\sum_{l_1,l_2}w_{l_1l_2}\sum_{m_1,m_2}g_{l_1l_2m_1m_2}2\,\mathrm{Re}(a_{-q_0l_1m_1}a_{q_0l_2m_2})\Bigg\}\end{aligned} \tag{5.5}$$

and

$$\frac{\Omega_{\rm int}^{(\rm LR)}}{V}=-\frac{16\pi^2}{9}\rho^2m^2\left[1-\frac{3}{q_0L}-\frac{(q_0\sigma)^2}{10}\right][|a_{q_010}|^2-\tfrac{1}{2}(|a_{q_011}|^2+|a_{q_01\bar{1}}|^2)-3\,\mathrm{Re}(a_{q_011}a_{q_01\bar{1}})]\ . \tag{5.6}$$

Terms of the order of $L^{-2\nu}$, $L^{3(\nu-1)}$, and L^{-1} have been neglected. The various coefficients are given by Eq. (3.11),

$$v_l=-\frac{1}{\beta}\frac{C(ll0,000)}{\sqrt{4\pi}}\int_{\sigma}^{\infty}dr\,r^4\hat{f}_{ll0}(r)\ , \tag{5.7}$$

$$w_{l_1l_2}=-\frac{1}{2\beta}C(l_1l_22,000)\left[\frac{5}{4\pi}\right]^{1/2}\int_{\sigma}^{\infty}dr\,r^4\hat{f}^{(\rm SR)}_{l_1l_22}(r)\ , \tag{5.8}$$

and

$$g_{l_1l_2m_1m_2}=\frac{C(l_1l_22,m_1m_2m)}{C(l_1l_22,000)}\frac{[(2-m)!(2+m)!]^{1/2}}{(2-m)!!(2+m)!!}\ , \tag{5.9}$$

where $\hat{f}^{(\mathrm{SR})}_{l_1 l_2 l}(r)=\hat{f}_{l_1 l_2 l}(r)$ for $(l_1 l_2 l)\neq(112)$ and

$$\hat{f}^{(\mathrm{SR})}_{112}=\hat{f}_{112}(r)=(4\pi)^{3/2}\sqrt{2/15}\beta m^2/r^3$$

[see Eq. (3.12)]. The entropic term [Eq. (2.2)] is more difficult to determine because the orientational distribution $\alpha(\mathbf{r},\omega)$ does not enter bilinearly as in the interaction contribution but as the argument of the logarithm. If the logarithm is expanded around the isotropic configuration $\alpha(\mathbf{r},\omega)=1/(4\pi)$ one finds

$$S=\sum_{n=2}^{\infty}\frac{(4\pi)^{n-1}(-1)^n}{n(n-1)}\times\int_{-1/2}^{1/2}dy\int d\omega\left[\sum_{qlm}{}'a_{qlm}e^{iqLy}Y_{lm}(\omega)\right]^n=\sum_{n=2}^{\infty}S^{(n)}\,. \tag{5.10}$$

The prime at the summation sign indicates that the term $l=0$ is to be omitted. Using the orthogonality of the spherical harmonics the term with $n=2$ can be expressed as

$$S^{(2)}=2\pi\sum_{q_1,q_2}\sum_{l,m}{}'\frac{\sin[(q_1-q_2)L/2]}{(q_1-q_2)L/2}a_{q_1lm}a^{*}_{q_2lm}$$
$$=2\pi\sum_{l,m}{}'\left[|a_{0lm}|^2+2|a_{q_0lm}|^2+\frac{\sin q_0L}{q_0L}2\,\mathrm{Re}(a_{q_0lm}a^{*}_{-q_0lm})+\frac{\sin q_0L/2}{q_0L/2}4\,\mathrm{Re}(a^{*}_{0lm}a_{q_0lm})\right]\,. \tag{5.11}$$

The expressions for $S^{(n\geq 3)}$ can be obtained from Eq. (5.10) by expanding the multinomial expression and integrating term by term, but for increasing n these expressions become very lengthy. In the spirit of the previous sections we reduce the number of parameters by taking into account only the terms with $l=1$. The average magnetization is given by

$$\langle\mathbf{M}\rangle=V^{-1}\int_V d^3r\,\mathbf{M}(\mathbf{r})$$
$$=\sqrt{4\pi/3}\rho m(-\sqrt{2}\,\mathrm{Re}a_{011},\sqrt{2}\,\mathrm{Im}a_{011},a_{010})+O(L^{-\nu})$$

so that in the thermodynamic limit $\langle\mathbf{M}\rangle$ is determined by the coefficients a_{01m}. From now on we study the case of zero external field which turned out to be especially interesting. (For the case $H\neq 0$ see the comment at the end of Sec. V B.) Then one would expect (and indeed it can be shown by numerical minimization) that the minimum of the bulk free energy is attained for $\langle\mathbf{M}\rangle=0$ which implies $a_{01m}=0$. Thus due to Eq. (5.2) besides q_0 there are six free parameters left. We parametrize the coefficients a_{q1m} as follows:

$$\begin{aligned}
&a_{q_010}=A_0e^{i\delta_0},\quad a_{-q_010}=A_0e^{-i\delta_0}\,,\\
&a_{q_011}=A_+e^{i\delta_+},\quad a_{-q_011}=-A_-e^{-i\delta_-}\,,\\
&a_{q_01\bar{1}}=A_-e^{i\delta_-},\quad a_{-q_01\bar{1}}=-A_+e^{-i\delta_+}\,,
\end{aligned} \tag{5.12}$$

with $A_0, A_\pm\geq 0$ and $\delta_0,\delta_\pm$ real so that the magnetization is given as [see Eqs. (3.15) and (5.3)]

$$\mathbf{M}(y)=\frac{4\pi}{3}\rho m\begin{bmatrix}-\sqrt{2}[-A_-\cos(q_0y+\delta_-)+A_+\cos(q_0y+\delta_+)]\\ \sqrt{2}[A_-\sin(q_0y+\delta_-)+A_+\sin(q_0y+\delta_+)]\\ 2A_0\cos(q_0y+\delta_0)\end{bmatrix}\,. \tag{5.13}$$

The *bulk* part of the interaction contribution then takes on the form

$$\left[\frac{\Omega_{\mathrm{int}}}{V}\right]_b=\tfrac{1}{4}\rho^2\hat{u}_0+6\pi\rho^2\hat{u}_1(A_0^2+A_-^2+A_+^2)-\frac{16\pi^2}{9}\rho^2m^2[A_0^2-\tfrac{1}{2}(A_-^2+A_+^2)-3A_+A_-\cos(\delta_+-\delta_-)] \tag{5.14}$$

and up to the order $n=4$ the entropic term is

$$S=4\pi(A_0^2+A_-^2+A_+^2)+\frac{24\pi^2}{5}[2A_-^4+2A_+^4+8A_-^2A_+^2+4A_-^2A_0^2+4A_+^2A_0^2+3A_0^4-4A_-A_+A_0^2\cos(\delta_-+\delta_+-2\delta_0)]\,. \tag{5.15}$$

In order to enable an analytical treatment we consider the limit of small anisotropy, i.e., $\rho \to \rho_{fc}$, where ρ_{fc} is the density of the second order phase transition to the isotropic phase. Then the quadratic terms of $(\Omega_{\rm int}/V)_b + (\rho/\beta)S$ dominate. Minimizing them under the constraint of fixed $C = A_0^2 + A_-^2 + A_+^2$ gives $\delta_+ - \delta_- = \pi$ and $A_- = A_+$ for *any* C. Therefore these conditions, which mean that the magnetization is *transversal,* must also be fulfilled at the unconstrained minimum. Incorporation of the fourth order terms then leads to $\delta_+ - \delta_0 = \pm\pi/2$ and $A_0^2 = 2A_+^2$. From Eq. (5.13) one finds that the magnetization vector describes a helical curve given by

$$\mathbf{M}(y) = 2\left[\frac{4\pi}{3}\right]^{1/2} \rho m A_0 \begin{pmatrix} \pm\sin(q_0 y + \delta_0) \\ 0 \\ \cos(q_0 y + \delta_0) \end{pmatrix} . \tag{5.16}$$

Thus the most stable configuration has a spatially constant absolute value of $\mathbf{M}$. This has been explicitly shown here, while it entered as an assumption in Sec. III. The phase δ_0 cannot be determined from the bulk terms, even if higher orders in S are included, since they are independent of δ_0 if the conditions found above are fulfilled. The value of A_0, which depends on the thermodynamic parameters ρ and T, follows from the minimization of

$$\frac{\Delta\Omega}{V} = \left[\frac{\Omega_{\rm int}}{V}\right]_b + \frac{\rho}{\beta} S$$
$$= 12\pi\rho^2 \left[\hat{u}_1 - \frac{8\pi}{27} m^2\right] A_0^2 + \frac{\rho}{\beta}\left[8\pi A_0^2 + \frac{192\pi^2}{5} A_0^4\right] . \tag{5.17}$$

This is equivalent to the minimization problem for the homogeneously magnetized long needle $[D(k=\infty)=0]$ in the same approximation [see Eq. (7.12) in Ref. [8] with $\alpha_{l\geq 2}=0$] if $\sqrt{12\pi}A_0$ is replaced by α_1, which corresponds to the same absolute value of the magnetization ($|\mathbf{M}| = 2\sqrt{4\pi/3}\rho m A_0 = \frac{2}{3}\rho m \alpha_1$). In particular the phase transition takes place at the same critical density

$$\rho_{fc}(T) = -\frac{2/3}{\beta[\hat{u}_1(T) - (8\pi/27)m^2]} = -\frac{2/3}{\beta u_1(T, k=\infty)} . \tag{5.18}$$

Numerical minimization shows that the above form of $\mathbf{M}(\mathbf{r})$ remains valid also at higher densities, i.e., for larger anisotropies.

By truncating the sum over q and l the above analysis has shown that the most favorable stripe configuration consists of a transversal helical structure whose amplitude is that for the equilibrium configuration in a long needle. In order to test the relevance of the truncation of the sum over l we consider a general, spatially constant, distribution

$$\tilde{\alpha}(\omega) = \frac{1}{2\pi}\sum_l \alpha_l P_l(\cos\theta) = \sum_l \mu'_{l0} Y_{l0}(\omega) \tag{5.19}$$

with $\mu'_{l0} = [\pi(2l+1)]^{-1/2}\alpha_l$ which is symmetric around the z axis. In the next step, from this distribution $\tilde{\alpha}(\omega)$ we generate a spatially varying distribution $\alpha(\mathbf{r},\omega)$ by applying local rotations along the y axis to $\tilde{\alpha}(\omega)$ such that the resulting coefficients $\mu_{lm}(y)$ lead to a magnetization

$$\mathbf{M}(y) = \tfrac{2}{3}\rho m \alpha_1 \begin{pmatrix} \cos q_0 y \\ 0 \\ \sin q_0 y \end{pmatrix} . \tag{5.20}$$

This means that we anticipate the helical structure found in Eq. (5.16). The expansion coefficients of this distribution $\alpha(y,\omega)$ are given by

$$\mu_{lm} = \sum_n D^l_{mn}(y)\mu'_{ln} = D^l_{m0}(y)\mu'_{l0} . \tag{5.21}$$

For a detailed discussion of the rotation matrices D^l_{mn} see Ref. [18]. In the present case the rotation corresponds to a rotation around the y axis by the angle $q_0 y$. According to Eq. (A106) in Ref. [18] this implies for Eq. (5.21) that one has

$$\mu_{lm}(y) = \left[\frac{4\pi}{2l+1}\right]^{1/2} Y^*_{lm}(q_0 y, 0)\mu'_{l0} . \tag{5.22}$$

From this expression the Fourier coefficients a_{qlm} defined in Eq. (5.3) can be inferred. For $l=1$ one finds

$$a_{q_0 10} = \frac{\mu'_{10}}{2}, \quad a_{q_0 11} = a_{q_0 1\bar{1}} = -\frac{\mu'_{10}}{2\sqrt{2}} i . \tag{5.23}$$

For $l \geq 2$ multiplies of q_0 up to lq_0 contribute to $\mu_{lm}(y)$. According to Eqs. (5.6) and (5.23) the bulk part of the long-ranged interaction contribution is

$$\lim_{V\to\infty} \frac{\Omega^{(\rm LR)}_{\rm int}}{V} = -\frac{8\pi^2}{9}\rho^2 m^2 \mu'^2_{10} = -\frac{8\pi}{27}\rho^2 m^2 \alpha_1^2 \tag{5.24}$$

as for a needle-shaped sample [8]. For the general ansatz in Eq. (5.1) it can be shown that the bulk part of the short-ranged interaction contribution is

$$\lim_{V\to\infty} \frac{\Omega^{(\rm SR)}_{\rm int}}{V} = \pi\rho^2 \sum_q \sum_{l,m} (2l+1)\hat{u}_l |a_{qlm}|^2 . \tag{5.25}$$

In the present case this expression can be simplified by using the fact that the sum of the absolute squares of all coefficients μ_{lm} with fixed l is invariant under rotations [see the discussion following Eq. (3.2)] so that

$$\sum_m |\mu_{lm}(y)|^2 = |\mu'_{l0}|^2 = \frac{1}{\pi(2l+1)}\alpha_l^2$$
$$= \sum_m \sum_{q_1,q_2} e^{i(q_1 - q_2)y} a_{q_1 lm} a^*_{q_2 lm}$$
$$= \sum_m \sum_q |a_{qlm}|^2 . \tag{5.26}$$

The last equation holds because the terms with $q_1 \neq q_2$ in the sum over q_1 and q_2 would lead to a y dependence which must vanish because $|\mu'_{l0}|^2$ is a constant. There-

fore one obtains

$$\frac{\Omega_{\rm int}^{(\rm SR)}}{V}=\rho^2\sum_l \hat{u}_l\alpha_l^2 , \tag{5.27}$$

again in agreement with the result for a homogeneously magnetized needle. As already noted in Sec. III the entropic term does not change if the orientational distribution is locally rotated. Thus we conclude that the stripe configuration in a cube obtained by the local rotations of the orientational distribution described by Eq. (5.20) has exactly the same bulk free energy as the spatially homogeneous configuration in a needle-shaped sample.

Since this result holds for any spatially constant configuration $\tilde{\alpha}(\omega)$ it is valid in particular for the configuration which minimizes the free energy of a needle-shaped sample. Thus we have proven that this stripe configuration renders the same *bulk* free energy as the configurations with $\mathbf{M}\cdot\mathbf{n}=0$ discussed in Sec. III for *any* value of q_0. Consequently the optimum value of q_0 (and thus ν) and the answer to the question whether this stripe configuration can compete with the domain configurations studied in Sec. III must be determined by those contributions to the free energy which are subdominant to the leading bulk term. If again one restricts oneself to the terms with $l=1$ and uses the helical solution Eq. (5.16) one derives from Eqs. (5.5), (5.6), and (5.10)

$$\frac{\Omega-\Omega_b}{V}=\frac{8\pi}{3}\rho^2 A_0^2[C_1(q_0L)^{-1}+C_2q_0^2] +O(L^{-2\nu},L^{3(\nu-1)},L^{-1}) \tag{5.28}$$

with

$$C_1=4\pi m^2,\quad C_2=-\tfrac{1}{2}v_1+\tfrac{1}{5}w_{11}+\frac{2\pi}{15}m^2\sigma^2 . \tag{5.29}$$

The entropic term gives no subdominant contributions; the terms with $\sin(q_0L)$ and $\sin(q_0L/2)$ in Eq. (5.5) vanish for the helical solution. Concerning possible finite size corrections to the coefficients a_{qlm} an argument analogous to the one given after Eq. (3.33) applies. Minimization of Eq. (5.28) with respect to q_0 gives the equilibrium wave number

$$q_0=\left[\frac{C_1}{2C_2L}\right]^{1/3} . \tag{5.30}$$

Therefore $q_0\sim L^{-1/3}$ so that $\nu=\frac{2}{3}$ in accordance with our assumption $0<\nu<1$. (The phase δ_0 does not appear in the next-order terms; its equilibrium value could only be determined if even higher-order terms were calculated.) From Eqs. (5.7), (5.8), and (5.29) one finds for small dipole moments

$$C_2=\frac{2\pi}{15}m^2\left[\sigma^2-2\int_\sigma^\infty dr\, r(e^{-\beta w_{\rm LJ}(r)}-1)\right]+O(m^6) . \tag{5.31}$$

The lowest-order term becomes negative if $T^*<1.47$ which would mean that the minimum of Eq. (5.28) is at $q_0=\infty$. We suspect that at such low temperatures this is a defect of our theory and do not pursue it further.

The power law found above also follows from the following simple argument. The magnetic energy of a cube of volume L^3 divided into stripe domains of width D is [23] $E_m\sim L^2DM^2$, while the energy of the domain walls is proportional to the product of the number of domains, the area of one wall, and the inverse domain thickness so that $E_w\sim L^3D^{-2}$. The last factor $\sim D^{-1}$ arises due to the continuous rotation of the magnetization direction across the whole domain (in contrast to Ising models or solid ferromagnets with easy axes of magnetization which cause microscopically thin domain walls). The power law $D\sim L^{1/3}$ can now be inferred by minimizing the sum of these competing energies. The comparison with Eq. (5.28) indicates that the terms with C_1 and C_2 correspond to the magnetic energy and the wall energy, respectively. From Eq. (5.30) the value of the grand canonical potential is

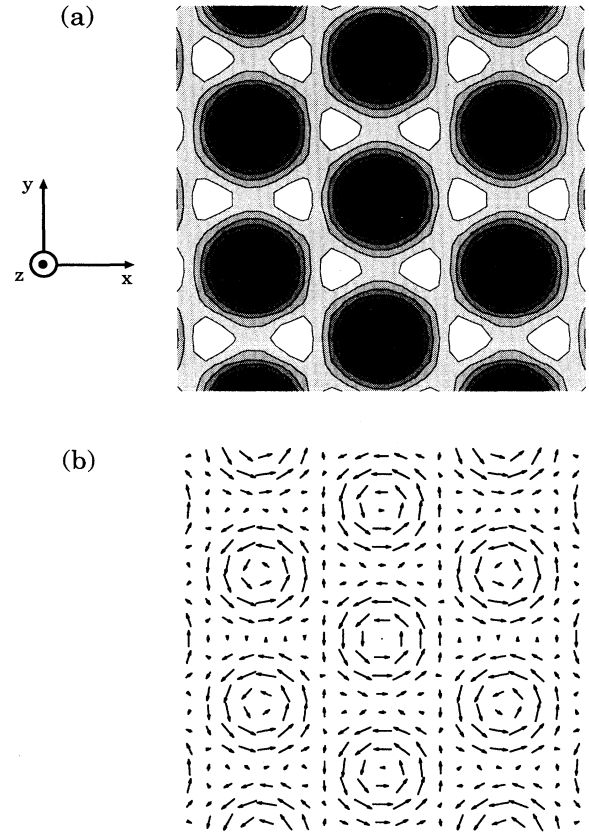

FIG. 15. Structure of the bubble phase. (a) Density plot of the z component of the magnetization, parallel to the tubular bubbles. In the black and dark gray regions M_z is positive and increases towards the axes of the bubbles, whereas in the white and light gray regions M_z is negative. (b) Field plot of the x and y components of the magnetization of the same configuration. The arrows indicate the x and y components of the magnetization of the same configuration. The arrows indicate the x and y components of $\mathbf{M}(x_0,y_0)$ where (x_0,y_0) corresponds to the center of each arrow. The configuration is translationally invariant in the z direction.

$$\Omega=\Omega_b+4\pi\rho^2 A_0^2(2C_1^2C_2)^{1/3}L^{7/3}+O(L^2)\ . \tag{5.32}$$

Since for large systems the positive contribution $\sim L^{7/3}$ dominates the terms proportional to the surface, i.e., $\sim L^2$, which occur for the domain configurations discussed in Sec. III, we conclude that in the thermodynamic limit the stripe phase is less favorable than the domains considered in Sec. III.

B. Bubbles

The bubble phase consists of a hexagonal array of tubular domains with a fixed direction of the magnetization (see Fig. 15). In the center of each domain the magnetization points in the same direction, which is parallel to the tubes. In the intervening region the magnetization is predominantly oriented in the opposite direction. This structure is described by the orientational distribution

$$\alpha(\mathbf{r},\omega)=\frac{1}{4\pi}+a_{00}Y_{10}(\omega)+\sum_{\mathbf{q},m}a_{\mathbf{q}m}e^{i\mathbf{q}\cdot\mathbf{r}}Y_{1m}(\omega)\ . \tag{5.33}$$

Here $\mathbf{q}$ takes on the six values $\pm\mathbf{q}_1,\pm\mathbf{q}_2,\pm\mathbf{q}_3$ with the reciprocal lattice vectors $\mathbf{q}_i$ given by

$$\mathbf{q}_1=q_0\begin{pmatrix}1\\0\\0\end{pmatrix},\quad \mathbf{q}_2=\frac{1}{2}q_0\begin{pmatrix}-1\\\sqrt{3}\\0\end{pmatrix},\quad \mathbf{q}_3=\frac{1}{2}q_0\begin{pmatrix}-1\\-\sqrt{3}\\0\end{pmatrix}, \tag{5.34}$$

so that $\alpha(\mathbf{r},\omega)$ is independent of z. The lattice constant is $4\pi/(\sqrt{3}q_0)$. In order to simplify the following calculations we have not taken into account terms $\sim Y_{lm}(\omega)$ with $l\geq 2$. Since α must be real and invariant under rotations around the z axis by $\pi/3$ one has

$$a_{\mathbf{q}m}=(-1)^m a^*_{-\mathbf{q}\bar{m}} \tag{5.35}$$

and

$$a_{-\mathbf{q}_{j-1}m}e^{im\pi/3}=a_{\mathbf{q}_j m}\ . \tag{5.36}$$

Due to these conditions the coefficients $a_{\mathbf{q}m}$ can be parametrized by four real parameters a_{00}, B_0, B_+, and δ_+ such that $a_{\mathbf{q}_1 0}=B_0$ and $a_{\mathbf{q}_1 1}=B_+e^{i\delta_+}$. Again we assume that $q_0\sim L^{\nu-1}$ for large L. A lengthy calculation yields as the bulk contributions to the density functional

$$\frac{\Omega_{\rm int}}{V}=\tfrac{1}{4}\rho^2\hat{u}_0-\frac{16\pi^2}{9}\rho^2m^2(B_0^2-B_+^2+3B_+^2\cos2\delta_+)+2\pi\rho^2\hat{u}_1(a_{00}^2+6B_0^2+12B_+^2)\ , \tag{5.37}$$

$$\frac{\Omega_H}{V}=-\left[\frac{4\pi}{3}\right]^{1/2}\rho mHa_{00}\ , \tag{5.38}$$

and

$$S=\sum_{n=1}^{\infty}\frac{(12\pi)^n}{(2n-1)2n(2n+1)}\sum_{j=0}^{2n}\sum_{i=0}^{[n-j/2]}b_{ij}^{(n)}B_+^{2i}B_0^j a_{00}^{2n-2i-j}\ . \tag{5.39}$$

We have determined the coefficients $b_{ij}^{(n)}$ in the entropic term up to $n=6$; here we give only the first two terms:

$$S=2\pi(a_{00}^2+6B_0^2+12B_+^2)+\frac{12\pi^2}{5}(216B_+^4+120B_+^2B_0^2+90B_0^4+48B_+^2B_0a_{00}+48B_0^3a_{00}+24B_+^2a_{00}^2+36B_0^2a_{00}^2+a_{00}^4)\ . \tag{5.40}$$

[Due to the complications induced by the dependence of $\alpha(\mathbf{r},\omega)$ on two spatial coordinates we have not yet determined the next-order contributions to the density functional.] Since only $\Omega_{\rm int}$ depends on δ_+ minimization immediately gives $\delta_+=0$ or π. The magnetization, given by an obvious generalization of Eqs. (5.3) and (3.15), then takes on the form

$$\mathbf{M}(\mathbf{r})=\left[\frac{8\pi}{3}\right]^{1/2}\rho m\begin{pmatrix}\pm B_+[\sqrt{3}\sin(\mathbf{q}_2\cdot\mathbf{r})-\sqrt{3}\sin(\mathbf{q}_3\cdot\mathbf{r})]\\ \pm B_+[2\sin(\mathbf{q}_1\cdot\mathbf{r})-\sin(\mathbf{q}_2\cdot\mathbf{r})-\sin(\mathbf{q}_3\cdot\mathbf{r})]\\ \sqrt{2}B_0[\cos(\mathbf{q}_1\cdot\mathbf{r})+\cos(\mathbf{q}_2\cdot\mathbf{r})+\cos(\mathbf{q}_3\cdot\mathbf{r})]+(1/\sqrt{2})a_{00}\end{pmatrix}\ .$$

The constants B_0 and B_+ are determined by numerical minimization. Figure 15(a) indicates the variation of the z component of the resulting magnetization configuration while Fig. 15(b) displays the corresponding x and y components. The magnetization is always perpendicular to a path connecting the centers of two neighboring bubbles. The helical variation of the magnetization along such a path is completely analogous to the one found for the stripe phase. For zero external field the critical density for the phase transition from the isotropic phase to the domain phase turns out to be the same for the stripe and bubble configurations. But the numerical evaluation of the density functional as well as an expansion for small deviations from the transition point indicate that the stripe phase is already more stable if only the bulk terms are considered. For finite external fields, however, the bubble phase is preferred near the phase transition and only at higher densities does a first order transition to the stripe phase take place. These results are in full accordance with the findings in Refs. [22] and [21]. But a com-

parison with the domain phase discussed in Sec. IV for $H \neq 0$ (using the same approximation, i.e., keeping only terms with $l=1$) shows that the bubble phase has the higher bulk free energy.

In summary, we can state that both the stripe and bubble phases have to be discarded as compared with the domain structures discussed in Secs. III and IV. Thus the structures found for dipolar Ising systems are not stable in the present system, in which the magnetization may point in any direction.

VI. SUMMARY

The following main results have been obtained.

(1) The magnetization curves in the case of a vanishing demagnetization factor (i.e., for needle-shaped samples or in the presence of infinitely permeable surroundings), for which the magnetization is homogeneous, are shown in Fig. 1.

(2) The phase diagrams of needle-shaped samples in external fields (Fig. 2) exhibit two critical points, the one at higher densities stemming from the tricritical point in zero field. The second order phase transition in zero field between the isotropic and the ferromagnetic liquid is washed out by the external field but remains discernible (Fig. 3).

(3) A detailed discussion of the comparison between our analytic results and published simulation data is presented at the end of Sec. II.

(4) If in a sample with arbitrary shape an inhomogeneous orientational distribution of the magnetization $\mathbf{M}$ is constructed from a homogeneous one by local rotations in such a way that $\nabla \cdot \mathbf{M}=0$ everywhere and $\mathbf{n} \cdot \mathbf{M}=0$ on the surface, the resulting configuration has the same bulk free energy as the corresponding homogeneous configuration in a long needle. In this case the demagnetization field [Eq. (3.19)] is zero. This result indicates that the bulk free energy is shape independent for $H=0$.

(5) The surface contributions to the free energy for the layered structure displayed in Fig. 8 have been calculated and it is has been shown that they are equal to the sum of the individual surface tensions at the different interfaces. From these results we conclude that the most stable configuration in a cube under the constraint of sharp domain boundaries is the triangular structure shown in Fig. 10.

(6) If an external field is applied perpendicular to the plane of the spontaneous zero field magnetization a rotation of $\mathbf{M}$ into the field direction is induced. This leads to a phase transition from an inhomogeneously magnetized phase at low fields to a homogeneously magnetized phase at high fields. In the domain phase the magnetization component parallel to the field increases linearly with H and is independent of T [see Eq. (4.7) and Figs. 11 and 12].

(7) Figure 13 displays the phase diagrams in the presence of an external field. For finite demagnetization factors there is a tricritical point and a line of second order phase transitions also for $H>0$. In this case the phase diagram does depend on the shape of the sample.

(8) The most stable stripe configuration exhibits a helical variation of the magnetization direction [Eq. (5.16)]. This configuration has the same bulk free energy as those with $\mathbf{n} \cdot \mathbf{M}=0$ at the surfaces. The width of the stripes scales as $L^{1/3}$ as a function of the system size L, which leads to contributions to the free energy proportional to $L^{7/3}$. Therefore, in contrast to dipolar Ising systems, the stripe configuration is unstable in the thermodynamic limit.

(9) The bubble structure depicted in Fig. 15 is less stable than the stripes at $H=0$ and less stable than the domain structures discussed in point (6) for $H \neq 0$.

As a continuation of this work we are studying a *free* numerical minimization of the density functional. Modern minimization methods, such as simulated annealing or conjugated gradients, allow a large number (10^4–10^6) of free parameters to be included. With this approach we especially want to study the structure of the domain boundaries and the behavior of the magnetization near the line singularities, which we expect to occur at the center of square or circular cylinders. The present analytic results will serve as important guidelines for these more detailed studies.

ACKNOWLEDGMENTS

S.D. would like to acknowledge the warm hospitality of M. Schick and of the Department of Physics at the University of Washington, Seattle, where he stayed during the preparation of this paper.

[1] D. Wei and G. N. Patey, Phys. Rev. Lett. **68**, 2043 (1992).
[2] D. Wei and G. N. Patey, Phys. Rev. A **46**, 7783 (1992).
[3] J. J. Weis, D. Levesque, and G. J. Zarragoicoechea, Phys. Rev. Lett. **69**, 913 (1992).
[4] J. J. Weis and D. Levesque, Phys. Rev. E **48**, 3728 (1993).
[5] M. J. Stevens and G. S. Grest, Phys. Rev. E **51**, 5962 (1995).
[6] M. J. Stevens and G. S. Grest, Phys. Rev. E **51**, 5976 (1995).
[7] B. Groh and S. Dietrich, Phys. Rev. Lett. **72**, 2422 (1994); **74**, 2617 (1995).
[8] B. Groh and S. Dietrich, Phys. Rev. E **50**, 3814 (1994).
[9] R. B. Griffiths, Phys. Rev. **176**, 655 (1968).
[10] H. Zhang and M. Widom, Phys. Rev. E **49**, R3591 (1994).
[11] P. G. de Gennes and P. A. Pincus, Solid State Commun. **7**, 339 (1969).
[12] A. Arrott, Phys. Rev. Lett. **20**, 1029 (1968).
[13] P. J. Wojtowicz and M. Rayl, Phys. Rev. Lett. **20**, 1489 (1968).
[14] M. Seul and D. Andelman, Science **267**, 476 (1995).
[15] P. Frodl and S. Dietrich, Phys. Rev. A **45**, 7330 (1992).
[16] D. Boda, I. Szalai, and J. Liszi, J. Chem. Soc. Faraday Trans. **91**, 889 (1995).
[17] M. E. Rose, *Elementary Theory of Angular Momentum*

(Wiley, New York, 1957).
[18] C. G. Gray and K. E. Gubbins, *Theory of Molecular Fluids* (Clarendon, Oxford, 1984).
[19] W. F. Brown, Jr., Phys. Rev. **105**, 1198 (1957).
[20] R. Frowein and J. Kötzler, Z. Phys. B **25**, 279 (1976).
[21] D. Andelman, F. Brochard, and J.-F. Joanny, J. Chem. Phys. **86**, 3673 (1987).
[22] T. Garel and S. Doniach, Phys. Rev. B **26**, 325 (1982).
[23] C. Kittel, Phys. Rev. **10**, 965 (1946).

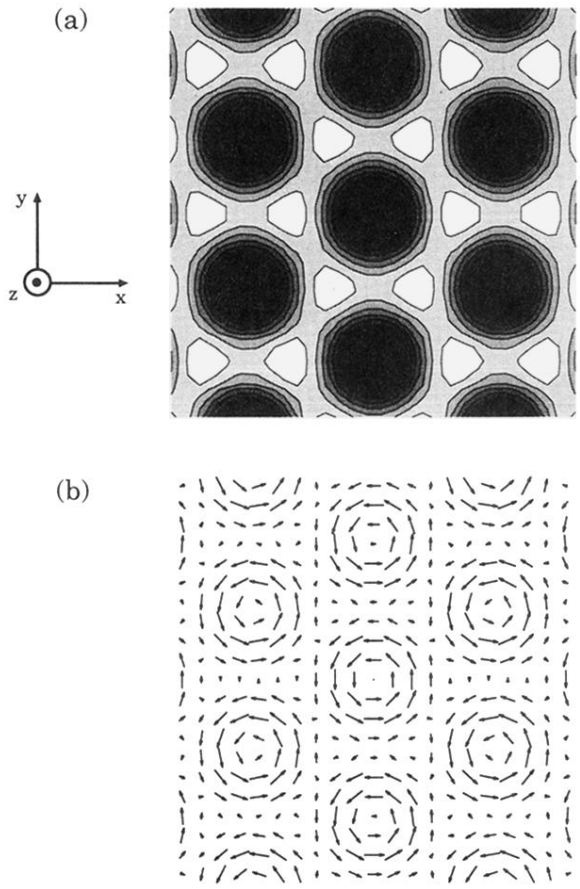

FIG. 15. Structure of the bubble phase. (a) Density plot of the z component of the magnetization, parallel to the tubular bubbles. In the black and dark gray regions M_z is positive and increases towards the axes of the bubbles, whereas in the white and light gray regions M_z is negative. (b) Field plot of the x and y components of the magnetization of the same configuration. The arrows indicate the x and y components of the magnetization of the same configuration. The arrows indicate the x and y components of $\mathbf{M}(x_0,y_0)$ where (x_0,y_0) corresponds to the center of each arrow. The configuration is translationally invariant in the z direction.